Planetary and Space Science 57 (2009) 1282–1301

Contents lists available at ScienceDirect

Planetary and Space Science

journal homepage: www.elsevier.com/locate/pss

The opposition effect in the outer Solar system: A comparative study of the phase function morphology

Estelle Déau [a,*], Luke Dones [b], Sébastien Rodriguez [a], Sébastien Charnoz [a], André Brahic [a]

[a] CEA/IRFU/Service d'Astrophysique, AIM UMR 7158, Orme des Merisiers Bâtiment 709, 91191 Gif-sur-Yvette, France
[b] Southwest Research Institute, 1050 Walnut Street, Suite 300, Boulder, CO 80302, USA

ARTICLE INFO

Article history:
Received 4 June 2008
Received in revised form
7 May 2009
Accepted 7 May 2009
Available online 15 May 2009

Keywords:
Planetary rings
Satellites of Jupiter, Saturn, Uranus, Neptune, phase curves
Opposition effect, coherent-backscattering and shadow-hiding, angular size of the solar radius

ABSTRACT

In this paper, we characterize the morphology of the disk-integrated phase functions of satellites and rings around the giant planets of our solar system. We find that the shape of the phase function is accurately represented by a logarithmic model [Bobrov, M.S., 1970. Physical properties of Saturn's rings. In: Dollfus, A. (Ed.), Surfaces and Interiors of Planets and Satellites. Academic, New York, pp. 376–461]. For practical purposes, we also parametrize the phase curves by a linear-exponential model [Kaasalainen, S., Muinonen, K., Piironen, J., 2001. Comparative study on opposition effect of icy solar system objects. Journal of Quantitative Spectroscopy and Radiative Transfer 70, 529–543] and a simple linear-by-parts model [Lumme, K., Irvine, W.M., 1976. Photometry of Saturn's rings. Astronomical Journal 81, 865–893], which provides three morphological parameters: the amplitude A and the half-width at half-maximum (HWHM) of the opposition surge, and the slope S of the linear part of the phase function at larger phase angles.

Our analysis demonstrates that all of these morphological parameters are correlated with the single-scattering albedos of the surfaces.

By taking more accurately into consideration the finite angular size of the Sun, we find that the Galilean, Saturnian, Uranian and Neptunian satellites have similar HWHMs ($\lesssim 0.5^\circ$), whereas they have a wide range of amplitudes A. The Moon has the largest HWHM ($\sim 2^\circ$). We interpret that as a consequence of the "solar size bias", via the finite angular size of the Sun which varies dramatically from the Earth to Neptune. By applying a new method that attempts to morphologically deconvolve the phase function to the solar angular size, we find that icy and young surfaces, with active resurfacing, have the smallest values of A and HWHM, whereas dark objects (and perhaps older surfaces) such as the Moon, Nereid and Saturn's C ring have the largest A and HWHM.

Comparison between multiple objects also shows that solar system objects belonging to the same planet have comparable opposition surges. This can be interpreted as a "planetary environmental effect" that acts to locally modify the regolith and the surface properties of objects which are in the same environment.

1. Introduction

The opposition effect is a nonlinear increase of brightness when the phase angle α (the angle between the source of light and the observer as seen from the body) decreases to zero. This effect was seen for the first time in Saturn's rings by Seeliger (1884) and Müller (1885). Now, this photometric effect has been observed on many surfaces in the solar system: first on satellites of the giant planets (Helfenstein et al., 1997; Kulyk, 2008); second on asteroids, (Harris et al., 1989a, b; Belskaya and Shevchenko, 2000) and Kuiper belt objects (Belskaya et al., 2008; Rosenbush et al., 2002; Schaefer et al., 2009); and finally on various surfaces on Earth (Verbiscer and Veverka, 1990; Hapke et al., 1996) and for minerals in the laboratory (Shkuratov et al., 1999; Kaasalainen, 2003). The opposition effect on bodies in the solar system has supplied interesting constraints about the regolith and state of the surfaces (Helfenstein et al., 1997; Mishchenko et al., 2006). Indeed, the opposition effect is now thought to be the combined effect of coherent backscatter (at very small phase angles), which is a constructive interference between photons (in a medium of grains with sizes near the wavelength of light), and shadow hiding (at larger phase angles), which involves shadows cast by the particles themselves (Helfenstein et al., 1997).

By parametrizing the morphology of the phase functions for $\alpha \sim 0$–20°, some numerical models have derived physical properties of the medium in terms of regoliths (Mishchenko and

* Corresponding author. Tel.: +33 1 69 08 80 56; fax: +33 1 69 08 65 77.
E-mail address: estelle.deau@cea.fr (E. Déau).

0032-0633/$ - see front matter © 2009 Elsevier Ltd. All rights reserved.
doi:10.1016/j.pss.2009.05.005

Dlugach, 1992a; Shkuratov et al., 1999) and the state of the macroscopic surface (Hapke, 1986, 2002; Shkuratov et al., 1999). However, such characterization of the phase function morphology is restricted by the angular resolution and the phase angle range of the observed phase function. Moreover, some effects (such as the finite size of the Sun and the nature of the soil), which are not yet taken rigorously into account by the most recent models, can play important roles in a comparative study.

For these reasons, it seemed important to test the behavior of the morphology of the phase function before using any physical model.

The use of a simple morphological model is generally not adapted to derive the physical properties of the studied medium. But for the data set presented here, only the disk-integrated brightness I/F and the phase angle α are available; the corresponding angles of incidence (i) and angles of emission (ε) are not given, so we cannot use sophisticated analytical models for further investigations (Hapke, 1986, 2002; Shkuratov et al., 1999), which need the brightness I/F and the three viewing geometry parameters α, μ and μ_0 (μ and μ_0 are the cosines of ε and i, respectively).

However, the theories developed for the coherent-backscattering and the shadow-hiding effects deduce their properties by parameterizing the opposition phase curve (Mishchenko and Dlugach, 1992a, b; Mishchenko, 1992; Shkuratov et al., 1999; Hapke, 1986, 2002). Thus it is possible to connect the morphological parameters A, HWHM and S with some physical characteristics of the medium derived from these models.

The amplitude A of the opposition peak is generally known to express the effects of coherent backscattering. According to Shkuratov et al. (1999) and Nelson et al. (2000), A is a function of grain size in such way that A decreases with increasing grain size (we refer to grains as the smallest scale of the surface compared to the wavelength and the virtual entities implied in the coherent-backscatter effect, as microscopic roughness). This anti-correlation finds a natural explanation in the fact that for a macroscopic surface, large irregularities with respect to the wavelength create less coherent effects than irregularities with sizes comparable to the wavelength.

Mishchenko and Dlugach (1992b) and Mishchenko (1992) emphasize that A is linked to the intensity of the background I_b (defined as a morphological parameter of the linear-exponential function of Kaasalainen et al., 2001), which is a decreasing function of increasing absorption (Lumme et al., 1990); thus A must increase with increasing absorption or decreasing albedo ϖ_0. This was confirmed by the laboratory measurements of Kaasalainen (2003). Indeed, Kaasalainen (2003) remarked that the opposition surge becomes stronger and narrower when irregularities are small and that the opposition surge decreases with increasing sample albedo (although some previous studies had reached the opposite conclusion, see Psarev et al., 2007).

The half-width at half-maximum, HWHM, is also associated with the coherent-backscatter effect. It has been related to the grain size, index of refraction, and packing density of regolith by previous studies (Mishchenko, 1992; Mishchenko and Dlugach, 1992a; Hapke, 2002). The variation of HWHM with these three physical parameters is complex; see Fig. 9 of Mishchenko (1993): HWHM reached its maximum for an effective grain size near $\lambda/2$ and increases when the regolith grains' filling factor f increases. For large values of f, the maximum of HWHM occurs for a larger grain size.

However, several studies (Helfenstein et al., 1997; Nelson et al., 2000; Hapke, 2002) defined two HWHM parameters: for the Hapke (2002) model, the coherent-backscatter HWHM (h_c), which is defined like that in the model of Mishchenko (1992), and the shadow-hiding parameter h_s. Applying this model to Saturn's rings, French et al. (2007) found that the coherent-backscatter peak is about 10 times narrower than the shadow-hiding peak, but neither h_c nor h_s equals the morphological width of the peak HWHM. This reinforces the idea that a coupling of the two opposition effect mechanisms at small phase angles could be responsible for the observed surge width.

Since the efficient regime of the shadow hiding is 0–40° (Buratti and Veverka, 1985; Helfenstein et al., 1997; Stankevich et al., 1999) and that of the coherent backscattering does not exceed several degrees (Helfenstein et al., 1997), the slope of the linear part S can be regarded as the only parameter that solely mirrors the shadow hiding. The slope is intrinsically negative since the phase function decreases with increasing phase angle in the backscattering direction, but we will discuss here the absolute values of S. The slope depends on the particle filling factor D, which relates to the porosity of the regolith of a satellite and the ratio between the particle size and the physical thickness of the ring for a planetary ring (Irvine, 1966; Stankevich et al., 1999; Kawata and Irvine, 1974). For a satellite, by "particles" we mean the macroscopic scales of the surface, which are implied in the shadow-hiding effect.

In the shadowing model of Irvine (1966) and Kawata and Irvine (1974) (which computes the effects of shadows for a single size of particles), the smaller the volume density D, the shallower the absolute slope S of the phase function between 3° and 6° (see Fig. 4 of Kawata and Irvine, 1974). By contrast, when the absolute slope is steep, the particle filling factor is higher and will contribute to a broad and large peak, which will be regarded as a steep linear part.

In a shadow-hiding model that considers shadowing by particles with a power-law size distribution, the wider the size distribution, the steeper the absolute slope S of the phase function between 1° and 6° (see Fig. 5 of French et al., 2007). However, at larger phase angles, the behavior of the absolute slope with the optical depth and size distribution could change according to a less efficient regime of the shadow hiding and the beginning of the multiple scattering domain (50–90°, Stankevich, 2008, *private communication*).

For a compact medium such as a satellite's surface, the slope at very large angles ($\alpha > 90°$) is a consequence of topographic roughness modeled by the so-called roughness parameter θ in the Hapke (1984, 1986) model. Then a steeper slope is due to a surface tilt which varies from millimeter to centimeter scales (Hapke, 1984). However, the roughness can influence the phase curve at smaller phase angles as underlined by Buratti and Veverka (1985). According to the laboratory measurements of Kaasalainen (2003), the slope of the phase function ($\alpha < 40°$) also increases with increasing roughness.

From the theoretical assertions made above, the HWHM and the amplitude A are governed by both coherent-backscatter and shadow-hiding effects, whereas the slope of the linear part of the phase curve only involves the shadow-hiding effect.

The goal of this paper is to understand the role played by the two known opposition effects (coherent backscatter and shadow hiding) on the morphology of the surge for different surface materials, which have different values of grain size, regolith grain filling factor, absorption factor (or inverse albedo), particle filling factor and vertical extension, by making some comparisons with their three morphological output parameters A, HWHM and S.

This paper describes the results of a full morphological parameterization and comparison of phase functions of the main satellites and rings of the solar system in order to compare the influence of parameters not yet implemented in actual models and simulations. Section 2 describes the data set that we use here and the specific treatment we added to these previously published data in order to compare them more easily. We also present the

morphological models and discuss their link with the physical properties of the surfaces. In Section 3, we focus on the behaviors of the derived morphological parameters, as a function of the single-scattering albedo, the distance from the Sun and the distance from the center of the parent planet and the general behaviors obtained after deconvolving. Section 4 is dedicated to a discussion in which we physically interpret the variations of the parameters *A* and *S*. Conclusions and future work that would be of interest are drawn in Section 5.

2. Data set description and reduction

2.1. The opposition effect around a selection of rings and satellites of the giant planets

We have applied a fitting procedure to a set of phase curves of satellites and rings obtained by previous ground-based and *in situ* optical observations (see Table 1 for references). In most cases, the spectral resolution of the filters used for these observations is not specified by their authors, and because we mix for some objects phase curves at similar wavelengths, we give an approximate value of the wavelength of observation (the uncertainty of the approximated values is roughly 100–200 nm).

For a comprehensive study of the morphology of the opposition phase curves, the solar phase curves of the Galilean satellites (Io, Europa, Ganymede and Callisto) and the jovian main ring were chosen, as well as the phase curves of the Saturnian rings (the classical A, B, and C rings and the tenuous E ring) and some Saturnian satellites (Enceladus, Rhea, Iapetus and Phoebe); the rings and satellites of Uranus [we will refer to the seven innermost satellites of Uranus—Bianca, Cressida, Desdemona, Juliet, Portia, Rosalind and Belinda—as the Portia group, to follow the designation of Karkoschka (2001). The phase function of the Portia group is then the averaged phase function for these seven satellites], including the Portia group and three other Uranian satellites, Titania, Oberon and Miranda; and finally two Neptunian ring arcs (Egalité and Fraternité) and two satellites of Neptune (Nereid and Triton). For all the satellites of this study, except for Iapetus which has a brighter trailing side, the phase function is representative of the leading side because they have, in general, better coverage at small phase angles. The references for the phase curves that we use in this study are given in Table 1.

This study aims to give an extensive comparison between rings around the giant planets (Jupiter, Saturn, Uranus and Neptune), as well as a comparison between rings and satellites for each giant planet of our solar system. For practical purposes, the well-known phase curve of the Moon is added as a reference.

Table 1
References for opposition phase curves of the selection of solar system rings and satellites.

Object	λ (nm)	References
Moon	~570	Whitaker (1969) and Rougier (1933)
Jupiter		
Main ring	~460	Throop et al. (2004)
Io	~570	McEwen et al. (1988)
Europa	~500	Thompson and Lockwood (1992)
Ganymede	~600	Morrison et al. (1974), Millis and Thompson (1975) and Blanco and Catalano (1974)
Callisto	~500	Thompson and Lockwood (1992)
Saturn		
C ring (HST)	672	French et al. (2007)
B ring	~650	Franklin and Cook (1965)
B ring (HST)	672	French et al. (2007)
A ring (HST)	672	French et al. (2007)
E ring	~650	Pang et al. (1983), Larson (1984) and Showalter et al. (1991)
Enceladus	439	Verbiscer et al. (2005)
Rhea	~500	Domingue et al. (1995) and Verbiscer and Veverka (1989)
Iapetus	~600	Franklin and Cook (1974)
Phoebe	~650	Bauer et al. (2006)
Uranus		
Rings	~500	Karkoschka (2001)
Portia *group*	~500	Karkoschka (2001)
Ariel	~600	Buratti et al. (1992) and Karkoschka (2001)
Titania	~600	Buratti et al. (1992) and Karkoschka (2001)
Oberon	~600	Buratti et al. (1992) and Karkoschka (2001)
Neptune		
Fraternité	~500	de Pater et al. (2005) and Ferrari and Brahic (1994)
Egalité	~500	de Pater et al. (2005) and Ferrari and Brahic (1994)
Nereid	~570	Schaefer and Tourtellotte (2001)
Triton	~400	Buratti et al. (1991)

2.2. Data set reduction

In order to properly compare the morphological parameters of the objects whose phase curves are given as magnitudes, we have converted the magnitude M to the disk-integrated brightness I/F by using

$$I/F \propto 10^{-0.4M} \quad (1)$$

(Domingue et al., 1995). This modification allows us to directly compare the slopes of the linear parts of all the curves with the same units.

2.3. Data set fits: the morphological models

The purpose of the present paper is to provide an accurate description of the morphological behavior of the observed phase curves. This is the very first step prior to any attempt to perform either analytical or numerical modeling. As a consequence, special care has been given here to parameterizing the observations efficiently and conveniently. In addition, morphological parameterization is necessary to compare numerous phase curves and derive statistical behavior, as will be done in Section 3.

Several morphological models have been used in the past to quantitatively describe the shape of the phase functions: the logarithmic model of Bobrov (1970), the linear-by-parts model of Lumme and Irvine (1976) and the linear-exponential model of Kaasalainen et al. (2001). The specific properties of these three models make them adapted for different and complementary purposes. The logarithmic model is an appropriate and simple representation of the data; the linear-by-parts model is convenient to describe the shape in an intuitive way; and finally, the linear-exponential model is commonly used for the phase curves of solar system bodies (see the comparative study of Kaasalainen et al., 2001).

2.3.1. The linear-by-parts model

For an intuitive description of the main features of the phase curves, the linear-by-parts model is the most convenient. It is constituted of two linear functions fitting both the surge at small phase angles (for $\alpha<\alpha_1$) and the linear regime at larger phase angles (for $\alpha>\alpha_2$), where, generally, $\alpha_1 \neq \alpha_2$. Besides α_1 and α_2, this function depends on four parameters, A_0, B_0, A_1, and B_1, such that

$$I/F(\alpha<\alpha_1) = -A_0 \cdot \alpha + B_0 \quad (2)$$

$$I/F(\alpha>\alpha_2) = -A_1 \cdot \alpha + B_1 \quad (3)$$

Lumme and Irvine (1976) and Esposito et al. (1979) use $\alpha_1 = 0.27^\circ$ and $\alpha_2 = 1.5^\circ$. By testing several values of α_1, it appears that for

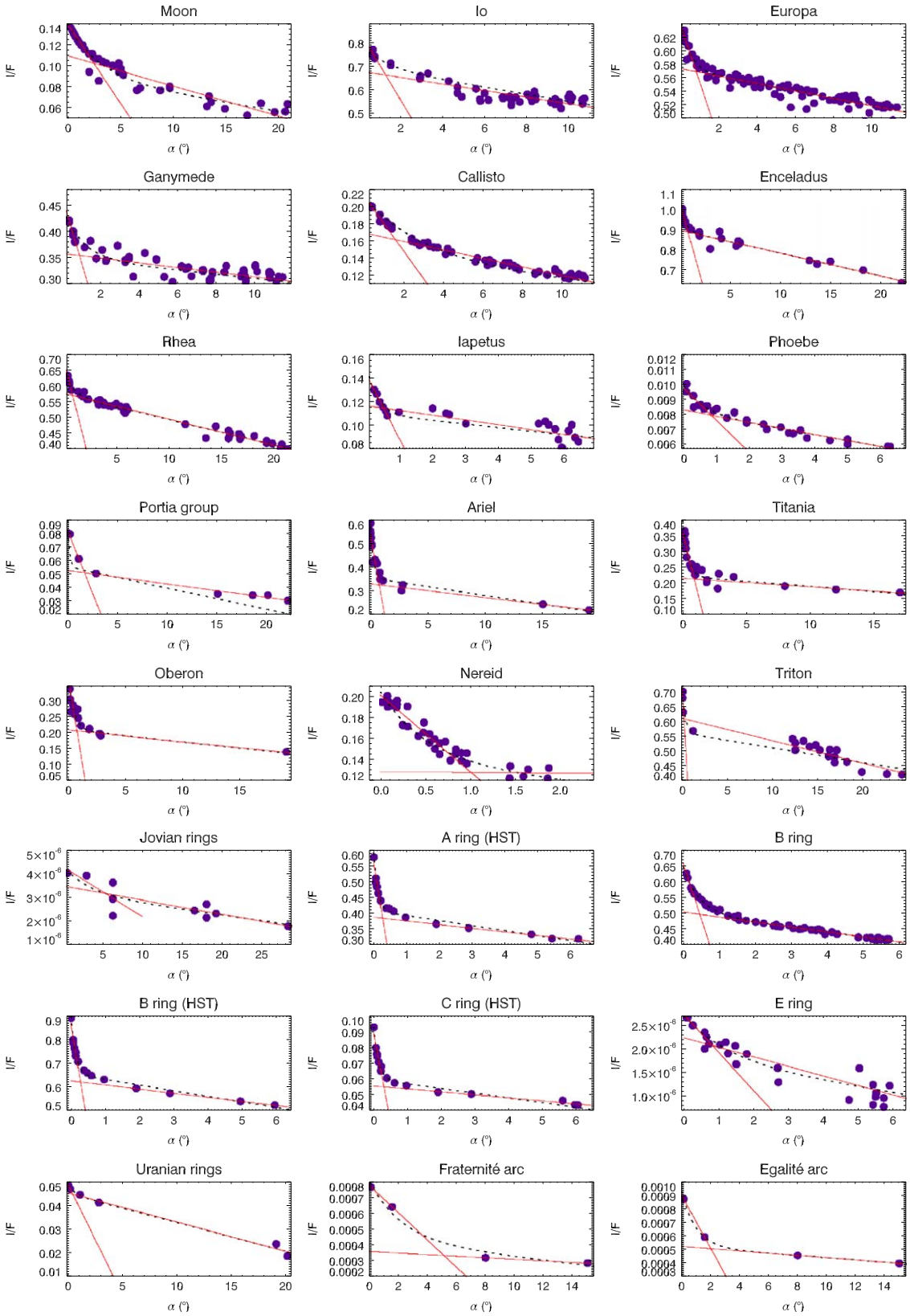

Fig. 1. Phase curves of a selection of rings and satellites in the solar system on a linear scale for phase angle (see Table 1 for references). The solid curves correspond to the best fit obtained with the linear-by-parts model and the dotted curves to the best linear-exponential fit.

our data set, values of $\alpha_1 = 0.5^\circ$ and $\alpha_2 = 2^\circ$ provide the best fits, so these values are adopted in the rest of the paper except for the Moon and tenuous rings for which we take $\alpha_1 = 1^\circ$.

Using the four parameters A_0, B_0, A_1 and B_1, the shape of the curve is characterized by introducing three morphological parameters: A, HWHM and S designating the amplitude of the surge,

the half-width at half-maximum of the surge, and the absolute slope at "large" phase angles (i.e., a few degrees up to tens of degrees), respectively. As a matter of fact, the slope of the linear part is intrinsically negative because of the decrease of the phase function with increasing phase angles. However, we define here S in an absolute way to better compare the values that will be found. The three morphological parameters are defined by

$$A = \frac{B_0}{B_1}, \quad \mathrm{HWHM} = \frac{(B_0 - B_1)}{2(A_0 - A_1)} \quad \text{and} \quad S = A_1 \tag{4}$$

Even if the entire phase curve near opposition cannot be fitted by two linear functions, this model offers a convenient description of the main trends of the phase variation (Fig. 1).

2.3.2. The linear-exponential model

The linear-exponential model describes the shape of the phase function as a combination of an exponential peak and a linear part. Its main interest is that it has been used in previous work for the study of the backscattering part of the phase curves of the solar system's icy satellites and rings (Kaasalainen et al., 2001; Poulet et al., 2002).

However, as noted by French et al. (2007), we find that this model does not fit the phase curves perfectly; in particular, A, HWHM and S are often under- or overestimated. In addition, the converging solutions found by a downhill simplex technique have large error bars, which means that a large set of solutions is possible and thus produce some difficulties for the comparison with the other objects.

For completeness, we calculate the four parameters of this model: the intensity of the peak I_p, the intensity of the background I_b, the slope of the linear part I_s and the angular width of the peak w such that the phase function is represented by

$$I/F = I_b + I_s \cdot \alpha + I_p \cdot e^{-\alpha/2w} \tag{5}$$

As $\alpha \to 0$, $\exp(-\alpha/2w) \to 1 - \alpha/2w + \mathcal{O}(\alpha^2)$, so that the slope approaches $I_s + I_p/(2w)$. The degeneracy of these parameters may explain some of the difficulty in obtaining good fits described above. For consistency with previous work, we can express the amplitude and HWHM of the opposition surge in this model as

$$A = \frac{I_p + I_b}{I_b}, \quad \mathrm{HWHM} = 2 \cdot \ln 2w \ \text{ and } \ S = -I_s \tag{6}$$

In Table 2 we report the morphological parameters of the linear-by-parts and the linear-exponential models (see also Fig. 1).

2.3.3. The logarithmic model

As noted by Bobrov (1970), Lumme and Irvine (1976) and Esposito et al. (1979), we remark that a logarithmic model describes the phase curves very well. It depends on two parameters (a_0 and a_1). This model has the following form:

$$I/F = a_0 + a_1 \cdot \ln(\alpha) \tag{7}$$

In general, this model is the best morphological fit to the data. However, a_0 and a_1 are not easily expressed in terms of A, HWHM and S, since the model's dependence on α is scale-free. We report the values of these two parameters in Table 3 to allow an easier reproduction of the observational data.

2.3.4. A method that takes into account the angular size of the Sun

For all the phase curves presented here, a comparison of their surges could be compromised because they have different values of their observed minimum phase angle values. For example, data for the Galilean satellites never reach phase angles lower than 0.1° whereas data for Saturn's rings almost reach 0.01°.

Table 2
Morphological parameters of original opposition phase curves of solar system objects.

Object	Linear-by-parts fit			Linear-exponential fit		
	A	HWHM	S	A	HWHM	S
Moon	1.27	1.21	0.0261	1.53	1.98	0.0017
Jupiter						
Main ring	1.23	2.68	0.0170	1.34	2.03	4.82×10^{-8}
Io	1.25	0.65	0.0204	1.14	0.83	0.01500
Europa	1.11	0.41	0.0095	1.13	0.31	0.0054
Ganymede	1.31	0.46	0.0125	1.28	0.69	0.0040
Callisto	1.25	0.78	0.0291	1.50	2.07	0.0024
Saturn						
C ring (HST)	1.61	0.15	0.0342	1.55	0.09	0.0030
B ring	1.30	0.23	0.0312	1.28	0.30	0.0155
B ring (HST)	1.38	0.14	0.0278	1.37	0.09	0.0238
A ring (HST)	1.44	0.13	0.0297	1.44	0.08	0.0159
E ring	1.22	0.40	0.0903	1.51	0.86	1.19×10^{-7}
Enceladus	1.15	0.42	0.0127	1.20	0.29	0.0113
Rhea	1.17	0.41	0.0142	1.14	0.52	0.0080
Iapetus	1.22	0.25	0.0348	1.36	0.22	0.0030
Phoebe	1.17	0.41	0.0485	1.20	0.38	0.0003
Uranus						
Rings	1.07	0.21	0.0274	1.08	0.45	0.0012
Portia *group*	1.80	0.20	0.0015	1.48	0.13	0.0015
Ariel	1.63	0.38	0.0178	1.60	0.18	0.0074
Titania	1.67	0.45	0.0126	1.82	0.27	0.0032
Oberon	1.77	0.37	0.0174	1.81	0.31	0.0037
Neptune						
Fraternité	2.16	2.57	0.0136	1.86	1.50	1.10×10^{-5}
Egalité	1.72	1.01	0.0160	1.77	0.67	8.34×10^{-6}
Nereid	1.56	0.50	0.0042	1.45	0.34	0.0099
Triton	1.17	0.10	0.0124	1.25	0.27	0.0049

The unit of HWHM is the degree and the unit of the slope S is $I/F\,\mathrm{deg}^{-1}$.

Although the behavior within the angular radius of the Sun represents a small part of the phase function, these smallest phase angles are crucial to constrain the fit, especially for the linear-exponential model. Indeed, when $\alpha \to 0$, the linear-exponential function tends toward $I_b + I_p$. As a consequence, this function flattens at very small phase angles.

However, in some cases this flattening does not correspond to the expected flattening due to the angular size of the Sun because the phase angle at which the linear-exponential model levels off depends upon the phase angle coverage. The less points there are at small phase angles, the sooner the flattening of the phase function occurs.

Déau et al. (2009) showed for Saturn's rings that the behavior of the surge observed by the Cassini spacecraft was accurately represented by a logarithmic model between 15° and 0.029°, where 0.029° corresponds to the angular size of the Sun at the time of the Cassini observations. Below 0.029°, the resulting phase function flattens, whereas the logarithmic function continues increasing. Considering the flattening specifically observed for Saturn's rings and generalizing for the solar system objects of this study, we were able to improve the treatment of the observed phase curves by creating extrapolated data points at very small phase angles. Indeed, it is more convenient to use extrapolated data points than to convolve the linear-exponential or the logarithmic functions with the solar limb darkening. This is the case because first, for inadequate phase angle coverage near exact opposition, the flattening of the linear-exponential function is almost uncontrollable and second, because for the logarithmic model, even if a convolution is possible, linking the morphological parameters A, HWHM and S to the outputs a_0 and a_1 is not trivial.

The method to create extrapolated data points consists of first fitting the logarithmic model to the data and then taking the value of the logarithmic function at the phase angle which corresponds to the solar angular size ($\alpha_\odot$, see Appendix). We then give to six points the same y-value: $I/F(\alpha = \alpha_\odot)$ and x-values ranging from 0.001° to $\alpha_\odot$ of phase angle. These extrapolated data points are represented in Fig. 2 (the full method is detailed in the Appendix). The extrapolated data and the original data are then fitted by the linear-exponential model in the last step.

For the Moon, Ariel and Oberon, for which the phase curve has a few points below the solar angular radius, we can see that the extrapolated points match the observational points quite well.

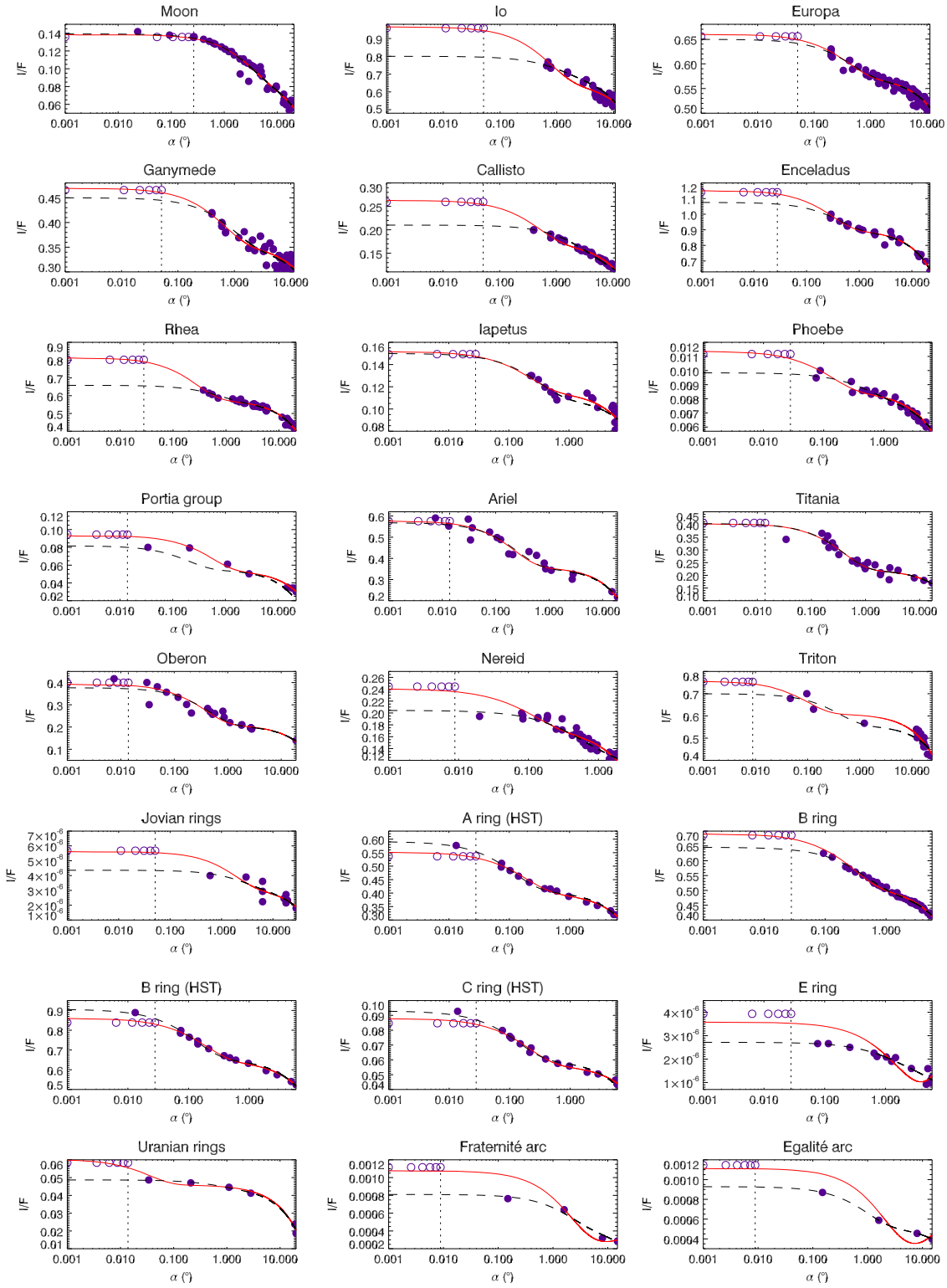

Fig. 2. Phase curves of a selection of rings and satellites in the solar system on a logarithmic scale for phase angle. The solid curves correspond to the best fit obtained with the linear-exponential model convolved with the size of the Sun (using extrapolated data below the angular size of the Sun, empty symbols) and the dashed curves correspond to the best linear-exponential fit (using only original data, filled symbols). The vertical dotted lines represent the angular size of the Sun at the observation time (see Table 6 of the Appendix).

This proves that the solar angular size effect flattens the phase functions below $\alpha_\odot$. In the case of the HST (Huble Space Telescope) data for Saturn's rings, for which we have also a few points below the solar angular radius, the extrapolated points have a bit smaller value than the observed points. This may be due to the fact that the data of French et al. (2007) already have been deconvolved to correct for scattered light.

We also performed a convolution of the linear-exponential function to a limb darkening function (see Appendix), but this refinement did not significantly change the values of *A*, HWHM and *S*, because the linear-exponential model already flattens as $\alpha \to 0$. Thus, by adding extrapolated data below $\alpha_\odot$, we are sure that the resulting fitting function will have a constant behavior below $\alpha_\odot$ and that the resulting fitting function will take into account the angular size of the Sun. Note that using this treatment, we assume that all bodies have a logarithmic increase up to the solar angular radius, which is only confirmed for Saturn's rings. Output parameters of our best fit for the "extrapolated linear-exponential" function are given in Table 3.

2.3.5. *A method of solar size deconvolution*

Although the behavior at phase angles smaller than the solar angular radius represents a small part of the opposition surge, a comparison of the surges of rings and satellites could be compromised because they have different values for the mean solar angular radius ($\alpha_{min} = 0.051^\circ$, 0.028°, 0.014°, 0.009°, respectively, for Jupiter, Saturn, Uranus and Neptune at their mean distances from the Sun). Indeed, according to the results presented here, the amplitude and HWHM seem linked to the finite angular size of the Sun. However, our morphological study does not clearly show that the Sun's angular size effect is preponderant for the amplitude *A*; the surges of Neptune's satellites have smaller amplitudes than those of Uranus (Fig. 8b). This contradicts the theoretical assumption that the solar angular size would give the largest amplitude to the most distant objects, for which the Sun has the smallest angular size. Because we previously noted that the finite size of the Sun would flatten the phase function when the phase angle was less than or equal to the solar angular radius (Déau et al., 2009), a naive deconvolution method would allow the phase curve to rise below $\alpha_\odot$. This is also suggested by a previous deconvolution of HST data on Saturn's rings, for which the brightness still increases below the phase angle $\alpha_\odot$ (French et al., 2007). However, the linear-exponential function is not appropriate for this purpose because it intrinsically flattens as $\alpha \to 0$. Thus the only morphological function that allows an increase, even at very small phase angles, is the logarithmic function. In particular, this function allows an increase of the brightness both above and below the solar angular radius (without a break in the brightness); thus using this function simulates a point source of light. However, we assume that the smallest phase angles are about $\alpha = 0.001^\circ$. In this way, if a physical flattening should be performed by the coherent-backscattering or the shadow-hiding effects, it will be possible at these phase angles.

The logarithmic function fits the phase function of Saturn's rings quite well at small and large phase angles (0.1–15°, Déau et al., 2009); however, none of the morphological parameters *A*, HWHM and *S* are well-defined in this model. Because the logarithmic model is a good representation of the data and performs a kind of deconvolution at phase angles less than $\alpha_\odot$, we fit these data by the linear-by-parts function. As shown in Fig. 3, the fitting results of this crude deconvolution method are reasonably acceptable when the phase function is plotted on a linear scale of phase angle.

Table 3
Direct output parameters of morphological models using original opposition phase curves and "ideal" opposition phase curves of solar system objects.

Object	Logarithmic fit		Linear-exponential fit				Extrapolated linear-exponential fit			
	a_0	a_1	I_p	I_b	w	I_s	I_p	I_b	w	I_s
Moon	0.114	−0.015	0.048	0.090	1.433	0.0017	0.049	0.088	1.548	0.0016
Jupiter										
Main ring	3.9×10^{-6}	-5.6×10^{-7}	1.1×10^{-6}	3.2×10^{-6}	1.470	4.8×10^{-8}	2.4×10^{-6}	3.2×10^{-6}	0.905	4.6×10^{-8}
Io	0.726	−0.077	0.100	0.699	0.600	0.0150	0.313	0.652	0.375	0.0107
Europa	0.580	−0.025	0.076	0.572	0.230	0.0054	0.086	0.573	0.193	0.0055
Ganymede	0.379	−0.028	0.100	0.349	0.500	0.0040	0.114	0.355	0.325	0.0041
Callisto	0.182	−0.025	0.070	0.140	1.500	0.0024	0.091	0.171	0.248	0.0051
Saturn										
C ring (HST)	0.056	−0.007	0.033	0.059	0.070	0.0030	0.031	0.056	0.104	0.0021
B ring	0.506	−0.050	0.142	0.502	0.223	0.0155	0.179	0.511	0.143	0.0174
B ring (HST)	0.628	−0.058	0.249	0.656	0.066	0.0238	0.213	0.647	0.094	0.0216
A ring (HST)	0.390	−0.046	0.182	0.409	0.060	0.0159	0.150	0.401	0.093	0.0143
E ring	2.1×10^{-6}	-5.2×10^{-7}	9.3×10^{-7}	1.8×10^{-6}	0.623	1.2×10^{-7}	4.8×10^{-7}	1.2×10^{-6}	1.085	3.8×10^{-7}
Enceladus	0.912	−0.063	0.180	0.895	0.215	0.0113	0.251	0.899	0.150	0.0116
Rhea	0.602	−0.055	0.085	0.573	0.379	0.0080	0.236	0.576	0.139	0.0082
Iapetus	0.112	−0.010	0.039	0.110	0.160	0.0030	0.035	0.116	0.111	0.0039
Phoebe	0.007	−0.0001	0.001	0.008	0.276	0.0003	0.002	0.008	0.067	0.0004
Uranus										
Rings	0.038	−0.004	0.003	0.044	0.326	0.0012	0.014	0.045	0.017	0.0012
Portia *group*	0.058	−0.006	0.026	0.055	0.100	0.0015	0.038	0.054	0.273	0.0010
Ariel	0.366	−0.044	0.213	0.355	0.129	0.0074	0.217	0.359	0.112	0.0077
Titania	0.252	−0.034	0.181	0.221	0.198	0.0032	0.181	0.221	0.198	0.0032
Oberon	0.236	−0.034	0.168	0.208	0.229	0.0037	0.181	0.211	0.186	0.0040
Neptune										
Fraternité	0.0005	−0.0001	0.00037	0.00043	1.082	1.1×10^{-5}	0.00086	0.00022	1.1×10^{-5}	5.6×10^{-6}
Egalité	0.0001	−0.001	0.00040	0.00052	0.489	8.3×10^{-6}	0.00090	0.00021	1.106	1.5×10^{-5}
Nereid	0.144	−0.021	0.064	0.140	0.250	0.0099	0.065	0.175	0.057	0.0301
Triton	0.584	−0.035	0.140	0.560	0.200	0.0049	0.146	0.609	0.049	0.0075

The unit of w is the degree and the unit of the slope I_s is $I/F\,\mathrm{deg}^{-1}$.

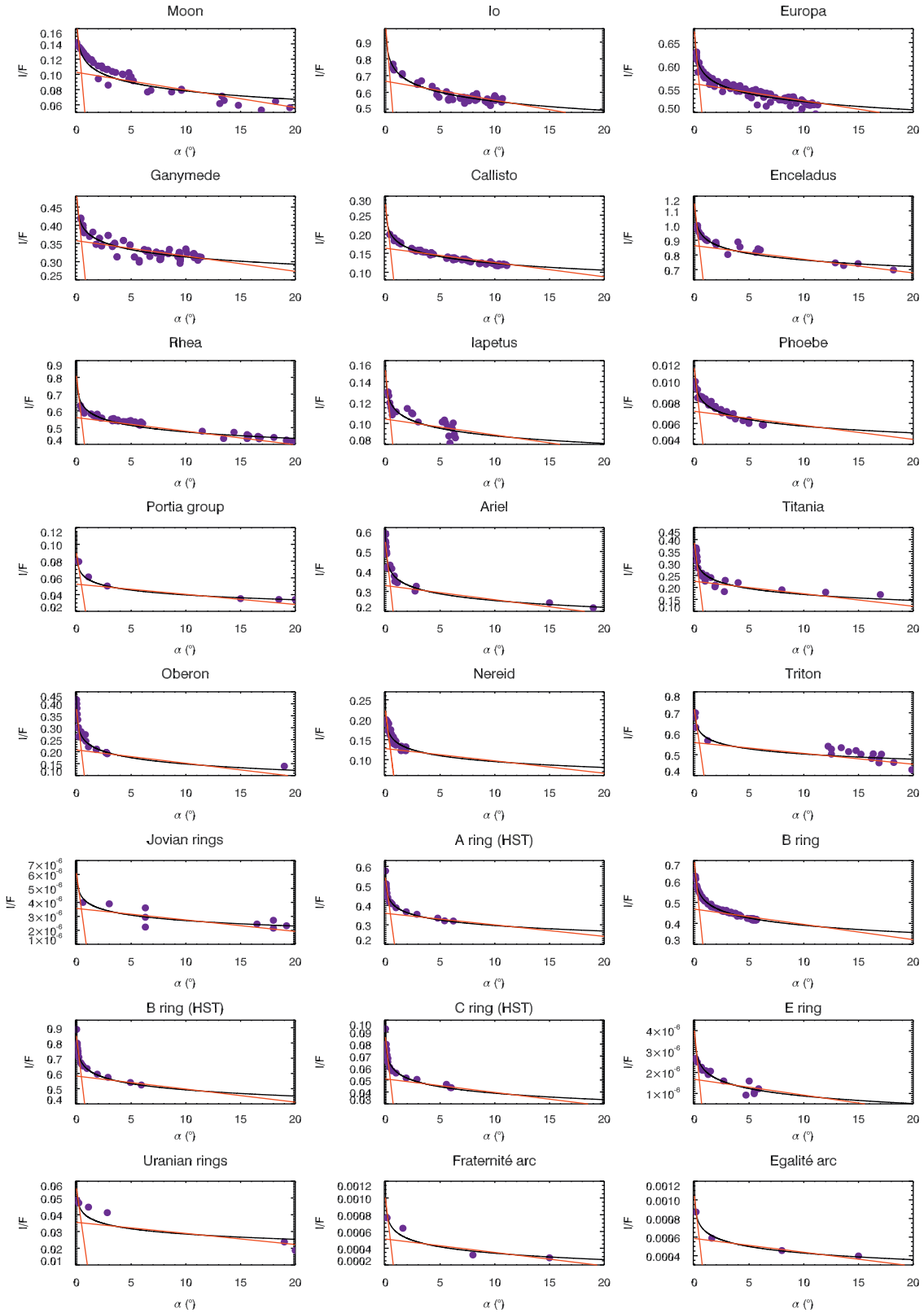

Fig. 3. Phase curves of a selection of rings and satellites in the solar system. The solid lines correspond to the best fit obtained with the linear-by-parts fit to the logarithmic model (in solid curves). Note that all panels cover the phase angle range 0–20°, unlike Figs. 1 and 2.

However, on a logarithmic scale of α, the linear-by-parts fit is obviously not acceptable because intrinsically, a linear function cannot fit a logarithmic increase. As a consequence, we have slightly changed the linear-by-parts parameters in order to take into account the slight flattening of this function. Because the y-intercept B_0 of the linear-by-parts model is less than the values

Table 4
Morphological parameters of "ideal" opposition phase curves of solar system objects.

Object	Linear-by-parts and log fits			Extrapolated linear-exponential fit		
	A	HWHM	*S*	*A*	HWHM	*S*
Moon	2.18	0.54	0.0224	1.55	2.14	0.0016
Jupiter						
Main ring	2.21	0.55	0.0230	1.76	1.25	4.55×10^{-8}
Io	1.89	0.41	0.0169	1.47	0.52	0.0107
Europa	1.34	0.16	0.0064	1.15	0.26	0.0055
Ganymede	1.62	0.29	0.0117	1.32	0.45	0.0041
Callisto	2.21	0.55	0.0229	1.53	0.34	0.0051
Saturn						
C ring (HST)	2.17	0.53	0.0221	1.54	0.14	0.0021
B ring	1.82	0.38	0.0155	1.35	0.19	0.0174
B ring (HST)	1.77	0.36	0.0146	1.32	0.13	0.0216
A ring (HST)	1.87	0.40	0.0165	1.37	0.12	0.0143
E ring	3.38	0.99	0.0450	2.80	1.50	3.76×10^{-7}
Enceladus	1.56	0.27	0.0107	1.27	0.20	0.0116
Rhea	1.76	0.35	0.0144	1.41	0.19	0.0082
Iapetus	1.76	0.36	0.0145	1.30	0.15	0.0039
Phoebe	1.99	0.45	0.0187	1.33	0.09	0.0004
Uranus						
Rings	1.98	0.45	0.0186	1.31	0.02	0.0012
Portia *group*	1.80	0.20	0.0015	1.71	0.37	0.0010
Ariel	2.13	0.52	0.0215	1.60	0.15	0.0077
Titania	2.21	0.55	0.0230	1.81	0.27	0.0032
Oberon	2.41	0.63	0.0267	1.86	0.25	0.0040
Neptune						
Fraternité	2.72	0.75	0.0314	4.99	1.53	5.61×10^{-6}
Egalité	2.39	0.62	0.0253	5.34	1.53	1.53×10^{-5}
Nereid	2.27	0.57	0.0241	1.37	0.08	0.0301
Triton	1.49	0.23	0.0092	1.23	0.06	0.0075

The unit of HWHM is the degree and the unit of the slope *S* is $I/F\,\mathrm{deg}^{-1}$.

of the logarithmic function when $\alpha < 0.01^\circ$, we replace B_0 by the value of the logarithmic function when $\alpha = 0.001^\circ$:

$$B_0' = a_0 + a_1 \cdot \ln(10^{-3}) \tag{8}$$

where $a_1 \leqslant 0$, in such a way that the amplitude and the angular width are now given by

$$A = \frac{B_0'}{B_1} \quad \text{and} \quad \mathrm{HWHM} = \frac{(B_0' - B_1)}{2(|a_1| - A_1)} \tag{9}$$

where $|a_1|$ is the absolute slope of the logarithmic function (see Section 2.3.3). Replacing $|a_1|$ by A_0 in the formula for HWHM was motivated by the fact that the original values of the linear-by-parts parameters were the same for all objects if we use the A_0 parameter (HWHM$\sim 0.22^\circ$ for $\alpha_1 = 0.3^\circ$). This is due to the fact that the logarithmic function is a fractal function, so it is not possible to obtain the half-width at half-maximum. Values of the linear-by-parts parameters *A*, HWHM and *S* are given in Table 4. Our best result is for the B ring, for which we previously found different values of *A* from the Franklin and Cook (1965) data and the French et al. (2007) data ($A = 1.30$ and 1.38, respectively, see Table 2 with the convolved models). The discrepancy was still present with the extrapolated linear-exponential model ($A = 1.35$ for Franklin and Cook, 1965, and $A = 1.32$ for French et al., 2007), due to the fact that the solar angular size was different at the two observation times (see Table 6 in the Appendix). Now, with the deconvolved model, the discrepancy of the two values is somewhat reduced compared to values from the fit to the original data: $A = 1.82$ for Franklin and Cook (1965) and $A = 1.77$ for French et al. (2007), Table 4, which implies that the angular size effect is now reduced.

3. Results

Our procedure is to carefully interpret the morphological results coming from a large number of phase curves. We start by studying the behaviors of the morphological parameters with the single-scattering albedo in the raw data and the improved data that take the angular size of the Sun into account (Sections 3.1 and 3.2). Then, by studying the behavior of the morphological parameters of the surge with the distance from the Sun and from the parent planet, we emphasize two additional effects that occur in the solar system: the "solar size bias" and the "planetary environmental effect" (Section 3.3). In the last step, we tried to eliminate the "solar size bias" by looking at the opposition effect in the outer solar system for an assumed point-source Sun (Section 3.4).

3.1. Behaviors of the morphological parameters

In this section we compare the morphological parameters as a function of the single-scattering albedo ϖ_0. What we call "single-scattering albedo" is technically the Bond albedo of a satellite or ring particle (Dones et al., 1993). Since the single-scattering albedo ϖ_0 represents the ratio of scattering efficiency to total light extinction over the entire phase angle range (Chandrasekhar, 1960), its value must be computed with the largest coverage of phase angle possible (0–180°). This is why we did not compute the single-scattering albedo with the phase curves presented in this paper, but use previously published values of single-scattering albedo computed from phase curves with a larger phase angle coverage and a wavelength close to our data. Thus, our references for phase curves (Table 1) and references for ϖ_0 (Table 5) are not always the same.

We did not find single-scattering albedo values for the jovian main ring and Saturn's E ring, so these two objects will be excluded from the study of the morphological parameters with the single-scattering albedo.

Table 5
References for the single-scattering albedos of solar system objects.

Object	ϖ_0	λ (nm)	References
Moon	0.21	~500	Helfenstein et al. (1997)
Jupiter			
Io	0.75	590	McEwen et al. (1988)
Europa	0.96	550	Domingue and Verbiscer (1997)
Ganymede	0.87	470	Domingue and Verbiscer (1997)
Callisto	0.53	470	Domingue and Verbiscer (1997)
Saturn			
C ring (HST)	0.16	672	French et al. (2007)
B ring	0.83	672	Poulet et al. (2002)
B ring (HST)	0.85	672	French et al. (2007)
A ring (HST)	0.79	672	French et al. (2007)
Enceladus	0.99	480	Verbiscer and Veverka (1991)
Rhea	0.86	480	Verbiscer and Veverka (1989)
Iapetus	0.16	480	Buratti (1984)
Phoebe	0.06	480	Simonelli et al. (1999)
Uranus			
Rings	0.06	~500	Karkoschka (2001)
Portia *group*	0,09	~500	Karkoschka (2001)
Ariel	0.64	~500	Karkoschka (2001)
Titania	0.48	~475	Veverka et al. (1987)
Oberon	0.43	~500	Karkoschka (2001)
Neptune			
Fraternité	0.02	480	Ferrari and Brahic (1994)
Egalité	0.02	480	Ferrari and Brahic (1994)
Nereid	0.21	~500	Thomas et al. (1991)
Triton	0.97	500	Lee et al. (1992)

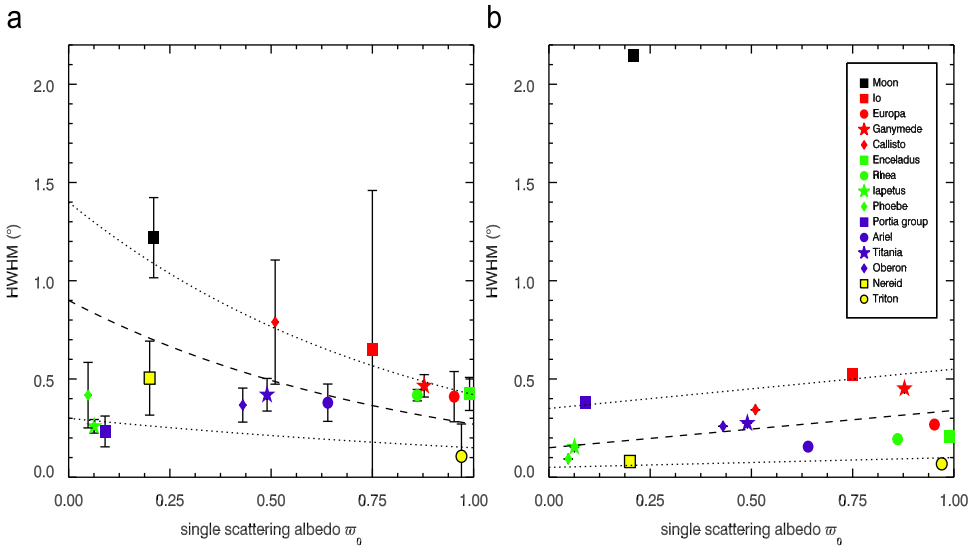

Fig. 4. HWHM of the surge for satellites of Jupiter, Saturn, Uranus and Neptune derived with: (a) the linear-by-parts model and (b) the linear-exponential model convolved with the size of the Sun. In (a) dashed line corresponds to a power-law fit to the data which is HWHM$\sim 0.9 \times 0.3^{\varpi_0}$. In (b) dashed line corresponds to a linear fit HWHM$\sim 0.15 + 0.19\varpi_0$. Dotted lines are empirical functions to the boundaries of the data.

3.1.1. Variation of the angular width of the surge with albedo

First, we discuss the variation of HWHM $= f(\varpi_0)$ derived from the linear-by-parts model (Fig. 4a) and HWHM $= f(\varpi_0)$ derived from the extrapolated linear-exponential model (Fig. 4b). Interestingly, the variation differs according to the morphological model: the first case leads to a decrease of HWHM when ϖ_0 increases, while the latter case leads to an increase of HWHM when ϖ_0 increases.

The main differences for HWHM $= f(\varpi_0)$ between the linear-by-parts results (well fitted by HWHM (degrees) $\sim 0.9 \times 0.3^{\varpi_0}$, Fig. 4a) and the extrapolated linear-exponential results (represented by HWHM (degrees) $\sim 0.15 + 0.19\varpi_0$, Fig. 4b) is mainly due to the points which correspond to the morphological parameters of the Moon, Callisto and Nereid. Indeed, in general, HWHM values from the extrapolated linear-exponential model significantly decrease from Figs. 4(a) to (b) for the outer solar system objects, whereas the value for the Moon increases by almost 1° between the two panels. This is due to the fact that when we take into account the Sun's angular size, this effect lowers the values of HWHM for the incomplete phase functions.

Independently from all these considerations, Fig. 4 shows a large dispersion of HWHM with albedo.

3.1.2. Variation of the amplitude of the surge with albedo

Fig. 5 shows a weak dependence of the amplitude of the surge on the albedo for the satellites, already noted by Helfenstein et al. (1997) and Rosenbush et al. (2002).

In both cases (linear-by-parts model, Fig. 5a, and extrapolated linear-exponential model, Fig. 5b) we note a dependence of A with ϖ_0, which follow a function leading to a decrease of A when ϖ_0 increases ($A \sim 1.65 \times 0.72^{\varpi_0}$ in Fig. 5a and $A \sim 1.75 \times 0.72^{\varpi_0}$ in Fig. 5b). The consistent trends in both cases imply that the finite size of the Sun was correctly accounted for with the help of the linear-by-parts model.

The decrease of A with increasing ϖ_0 could be understood through a relation between the amplitude and the single-scattering albedo via the intensity of the background phase function I_b (one of the parameter of the linear-exponential model). The intensity of the background phase function is believed to be inversely proportional to the albedo (Lumme et al., 1990; Mishchenko and Dlugach, 1992a). So the amplitude A of the surge should increase with increasing absorption, or decrease with increasing albedo. Thus, the predicted trend of Lumme et al. (1990) and Mishchenko and Dlugach (1992a) is confirmed by our present results.

In addition, Fig. 5b labels satellites by color to indicate their parent planet. This figure indicates that distant objects (such as the Uranian satellites) have a significantly larger amplitude than less distant objects (such as the Galilean or Saturnian satellites) while the Neptunian satellites have intermediate values. Then it must be considered that the finite size of the Sun has a role in the amplitude's value (Shkuratov, 1991). As a consequence, even if the trend of $A = f(\varpi_0)$ is well explained by theoretical considerations, one can remark that the large dispersion in this correlation could be due to other effects (such as the finite size of the Sun) that weakens the albedo dependence of A. Thus, as for HWHM, we cannot physically interpret their variation with albedo as long as they are biased by the effect of the solar angular size.

3.1.3. Variation of the slope of the linear part with albedo

The last morphological parameter is the slope S, which we represent as a function of the single-scattering albedo ϖ_0 for the rings (Fig. 6a) and satellites (Fig. 6b) of the solar system.

In this figure, rings and satellites have different values of slope as function of their albedo, and a slight increase for S with increasing ϖ_0 is noticed. For the rings (Fig. 6a), it seems that a good correlation appears between S and the albedo, which may be roughly fitted by a function like $S \sim 0.001 + 0.02 \cdot \varpi_0^2$. A similar fit works well for the satellites (the Moon, Saturnian and Uranian satellites are close to the dashed line in Fig. 6b). This fit to the points could be represented by the following function: $S \sim 0.001 + 0.01 \cdot \varpi_0^2$ (Fig. 6b). This correlation suggests that multiple scattering may be a strong element at play in the regime of self-shadowing (beyond ~1° of phase angle), in qualitative agreement with Kawata and Irvine (1974). However, we note that three objects fall far from our fitted curve: Europa, Ganymede and Io.

The positive correlation of the absolute slope S with the single-scattering albedo is given here in $I/F\,\mathrm{deg}^{-1}$ units. We investigate now the variation of a normalized slope (S' in deg^{-1} units) by defining it as the ratio of the absolute slope S over the parameter B_1, which is the y-intercept of the linear part at large phase angles ($\alpha > \alpha_2$). In this way, we obtain an absolute and normalized slope, as previously discussed by French et al. (2007) and Déau et al. (2009) for the study of Saturn's rings. The trends previously found

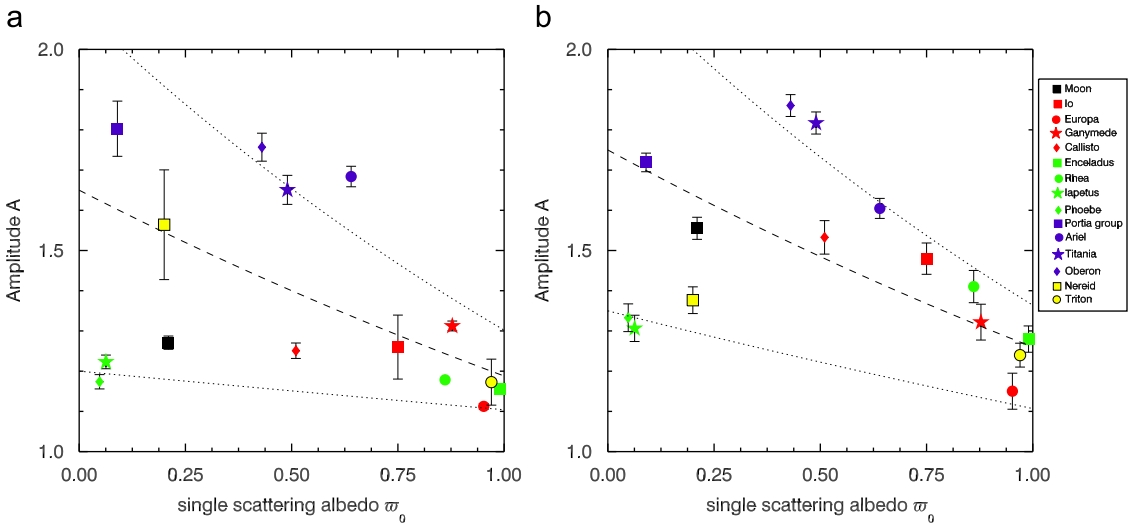

Fig. 5. Amplitude of the surge for satellites of Jupiter, Saturn, Uranus and Neptune: (a) the linear-by-parts model and (b) the linear-exponential model convolved with the size of the Sun. In (a) dashed line corresponds to a power fit to the data $A \sim 1.65 \times 0.72^{\varpi_0}$. In (b) dashed line corresponds to the fit $A \sim 1.75 \times 0.72^{\varpi_0}$. Dotted lines are empirical functions to the data boundaries.

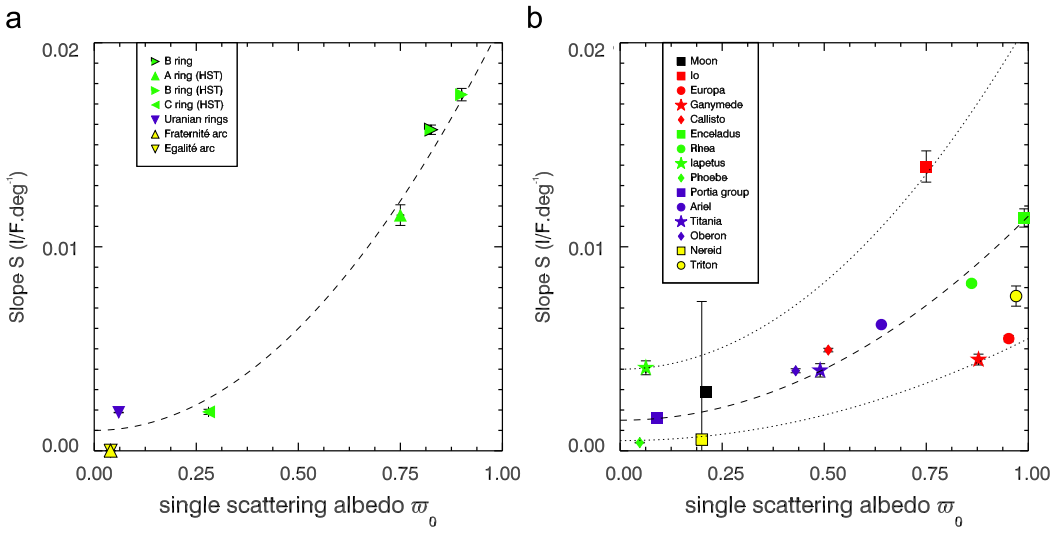

Fig. 6. Morphological parameter S derived with the linear-by-parts model for: rings (a) and satellites (b) of Jupiter, Saturn, Uranus and Neptune. In (a) dashed line corresponds to a power-law fit to the data which is $S \sim 0.001 + 0.02\varpi_0^2$. In (b) dashed line corresponds to a fit to the data which is $S \sim 0.001 + 0.01\varpi_0^2$. Dotted lines are empirical functions to the data boundaries.

are still the same, we found also an increase of S' with increasing single-scattering albedo for the rings ($S' \sim 0.001 + 0.045 \cdot \varpi_0^2$) and the satellites ($S' \sim 0.004 + 0.022 \cdot \varpi_0^2$).

3.2. *Cross comparisons between the morphological parameters of the surge*

We see in Fig. 4 that the angular width of the surge can change significantly by taking into account the solar angular radius. *However, this is not the case for the amplitude* (Fig. 5). Fig. 7 shows a cross comparison between the morphological parameters A and HWHM obtained with the linear-exponential model convolved (Fig. 7b) or not (Fig. 7a) with the limb darkening function.

In the first graph (Fig. 7a), two different groups may be qualitatively distinguished.

On the one hand, there is a group of bodies with similar values of the HWHM, in the range 0.1–0.4°, but with significantly different values of the amplitude, from 1.4 to 1.8. It is interesting to note that these bodies, which include the Saturnian rings and Uranian satellites, are not in the outermost part of the solar system (such as the Neptunian satellites). Within this group, we also note that similar bodies are clustered in the (A, HWHM) space: the Uranian satellites have, on average, the largest values of the amplitude, ~1.7. Saturn's rings have an amplitude between 1.3 and 1.6, closer to the Uranian satellites. We also note that whereas all satellites have quite a constant HWHM (between 0.2° and 0.4°), Saturn's rings have systematically lower values, between 0.08° and 0.09°, which may suggest a different state for their surface.

The second group includes Saturn's satellites, along with Io, Europa and Triton, which have the smallest values of amplitude. A very striking feature is the peculiar behavior of bodies such as

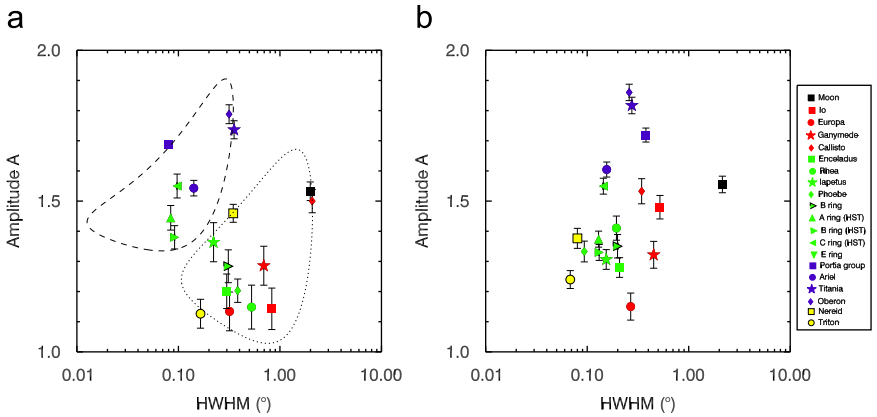

Fig. 7. Cross comparison between the morphological parameters of the surge derived with (a) the linear-exponential model and (b) the linear-exponential model convolved with the size of the Sun (see Tables 6 and 7 in the Appendix). Dashed and dotted curves in panel (a) are arbitrary delimitations of the data points (see text).

Callisto and the Moon: they have similar amplitudes (about 1.5) and also similar HWHMs (about 2°). In the second graph (Fig. 7b), it first seems that the bodies belonging to the same primary planet have similar values of A and HWHM. For the Galilean satellites, we found the largest HWHM for the outer solar system satellites (between 0.2° and 0.5°) and amplitude between 1.1 and 1.5. The Uranian satellites still have the largest amplitudes (A ranges between 1.6 and 1.9), but the values of HWHM are similar to those of those of Saturn's rings and satellites. The Neptunian satellites have the sharpest opposition peaks (HWHM $\lesssim 0.1°$) but moderate amplitudes (between 1.2 and 1.4), similar to the range of the Saturnian satellites.

Does this imply some deep structural difference of the surface regolith of bodies, or is it due to the Sun's angular size effect? For the moment we note that the opposition effect is poorly understood, especially at phase angles smaller than 1° in the coherent-backscattering regime.

Whereas physical implications are still hard to draw from these graphs, it is interesting to note that the solar angular size refinement that we use naturally clusters different kind of surfaces in different locations of the (A, HWHM) space, and that "endogenically linked objects" are quite well gathered in small regions of this space. This could suggest that common environmental processes (meteoroid bombardment, surface collisions, space weathering, etc.) may homogenize different surface states by processing mechanisms that may determine the microstructure of the surface. These mechanisms, in turn, may affect the behavior of the opposition surge at very low phase angles, as it may be linked with the spatial organization of micrometer-scale surface regolith (Mishchenko, 1992; Mishchenko and Dlugach, 1992a; Shkuratov et al., 1999).

3.3. Additional effects

With the help of the cross comparison of the surge morphological parameters, we noticed that two supplementary effects can significantly modify the values of A and HWHM: one purely of observational origin, the "solar size bias", and one other purely physical, the "planetary environmental effect" (the fact that objects seem to be endogenically linked).

3.3.1. The "solar size bias"

We tested the influence of the solar angular size by representing in Fig. 8 the morphological parameters of the surge A and HWHM as a function of the distance from the Sun d (in Astronomical Units).

We represent HWHM (Fig. 8a) and A (Fig. 8b) from the linear-by-parts model with filled symbols and that of the extrapolated linear-exponential model with outlined symbols.

We remark that the linear-by-parts angular width follows the power-law function HWHM (degrees) $\sim 0.33 + 1.1d^{-1.5}$ (the solid line in Fig. 8a). The fit is quite good from the Moon to Uranus, but is far from the HWHM values of Neptune's satellites (especially that of Nereid). It is easier to see with this representation that the HWHM of Nereid is larger than that expected from the power-law function. The extrapolated linear-exponential HWHM reduces this difference because the Neptunian satellites have in this case smaller values of HWHM that are better fitted by the power-law function. Indeed, the extrapolated linear-exponential HWHM follows a similar function (HWHM (degrees) $\sim 0.12 + 2.3d^{-1.4}$), but values in the extreme parts of the solar system (innermost with the Earth's satellite and outermost with Neptune's satellites) are significantly different: for the Moon, the extrapolated linear-exponential HWHM is larger than its linear-by-parts counterpart and for Nereid, the extrapolated linear-exponential HWHM is smaller than the linear-by-parts HWHM.

However, such a strong trend is not observed in the case of the amplitude of the surge. As shown in Fig. 8b, a fit to the linear-by-parts amplitudes is good for the Galilean, Saturnian and Uranian satellites (which we fitted by a linear function $A \sim 1.1 + 0.08d$), but not at all for the Moon and the Neptunian satellites. The predicted behavior (i.e., the dashed line in Fig. 8b) shows that the value for the Moon is overestimated and that the values of the Neptunian satellites are strongly underestimated. Previous work by Bauer et al. (2006) also underlined the fact that the amplitude of the Neptunian satellites did not follow the behavior of the Uranian ones. Indeed, by adding the surge amplitudes of other small bodies throughout the Solar system to their study of Saturnian irregular satellites, Bauer et al. (2006) showed that the Uranian satellites seem to have a slightly steeper surge than Neptune's moon Triton, which, in turn, has a similar value to main-belt, F-type asteroids. If the Uranian satellites, which have a wide range of values of amplitudes, are not taken into account, the work of Bauer et al. (2006) is compatible with a surge amplitude that increases slightly with heliocentric distance. We now use the values of the extrapolated linear-exponential amplitude A, but this did not improve the fit of A with distance from the Sun. Indeed, the extrapolated linear-exponential amplitude is larger than the linear-by-parts amplitude for the Moon, whereas the extrapolated linear-exponential values of the Neptunian satellites are smaller than their linear-by-parts counterparts. The exact opposition trends were expected to obtain a good linear fit from the Moon

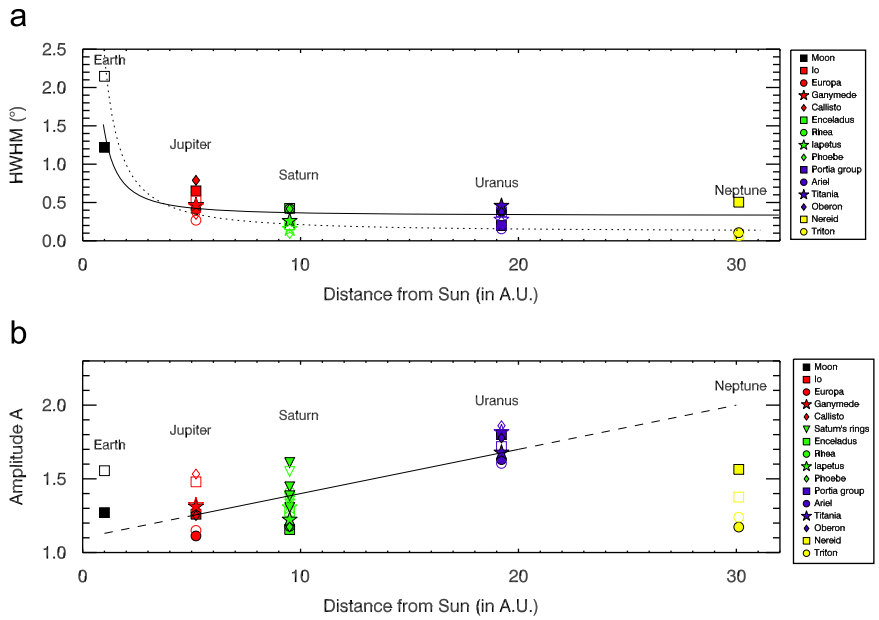

Fig. 8. Variation of the morphological parameters HWHM and *A* derived with the linear-by-parts model (filled symbols and solid line) and the extrapolated linear-exponential model (empty symbols and dotted line) with respect to the distance from the Sun (distances are taken from Murray and Dermott, 2000).

to Neptune. Perhaps the solar size effect is negligible at Neptune's distance and the values of *A* and HWHM are physical, in the sense that they depend only on the opposition effect mechanisms (coherent backscattering and shadow hiding).

These results seems to suggest that *A* is less affected by the "solar size bias" than HWHM, which is entirely controlled by this effect (which seems trivial because this bias is an angular effect). It is possible that the values of *A* result from a coupling of the physical opposition effects (coherent backscatter and shadow hiding) with the environmental opposition effects (solar and planetary). As a consequence, the deconvolution of the phase function (at least for the "solar size bias") should allow the physical opposition effects to express themselves fully in the values of *A* and HWHM.

3.3.2. *The "planetary environmental effect"*

A previous study by Verbiscer et al. (2007) has confirmed, at the scale of the Saturnian system, a kind of "endogenic" or "ecosystemic" classification of the opposition surge. Indeed, this work demonstrated that the opposition surge parameters of the innermost classical Saturnian satellites are a function of the distance from Saturn. Verbiscer et al. (2007) interpreted this trend as being due to "sandblasting" of the satellites by grains from the E ring, which encompasses the region between the orbits of Mimas and Rhea.

For the planetary environments of Jupiter, Uranus and Neptune, there are no significant variations in the surge parameters with distance from the parent planet. The first possible reason is statistical, because there are not enough data (for these systems, we have less than four moons). The second is that the dust environment can be influenced by other effects (e.g., the planet's magnetospheric activity, the satellite's activity, the proximity to the Kuiper belt and transneptunian objects) that might produce larger effects than any related to the distance from the parent planet.

For the Saturnian system, for which local interactions between satellites and rings exist, we observe trends similar to those found by Verbiscer et al. (2007) (see Fig. 9).

Variations of the morphological parameters on large distance scales (for the Saturn system) show trends that suggest a common ground for environmental processes. These processes may imply different surfaces, but will be handled by the opposition effect in the same way as the mechanisms that determine the micro-structure of the surface. According to theoretical models of coherent backscattering, the amplitude is related to the grain size and HWHM depends on the composition, distribution of grain sizes and the regolith filling factor. Thus the behavior of the opposition surge is connected to the spatial organization of the regolith (Mishchenko and Dlugach, 1992a; Shkuratov et al., 1999).

Therefore, the study of the morphology of the opposition peak can highlight dynamical interactions between the rings, satellites and the surrounding environment through the photometry. These ring/satellite interactions noted here go beyond the general dynamical interactions between rings and satellites (such as resonances, for example). Here these interactions involve common erosion histories on the surfaces of the rings and satellites. Similar values of HWHM, according to the theory of Mishchenko and Dlugach (1992a), can be explained by similar values of refractive index (with various values of grain size and filling factor), or by different values of refractive indices, but similar values of grain sizes and filling factor of the regolith.

There are two known mechanisms that can act together in order to explain the similarities in the values of HWHM for objects that are *endogenically linked*.

① The impacts of debris in planetary environments can change the chemical composition of the rings and satellites: new elements can be directly added to the system; the more volatile elements can be preferentially removed and the more fragile compounds can be preferentially processed. The work of Cuzzi and Estrada (1998), in particular, details the changes in the chemical composition of Saturn's rings induced by meteoroid bombardment and ballistic transport.

② The second mechanism that is likely to act concerns every kind of collisional mechanism capable of modifying, at microscopic scales, the surface of the satellite's regolith (meteoroid bombardment, external collisions, disintegration in space, etc.); see Lissauer et al. (1988) and Colwell and Esposito (1992, 1993).

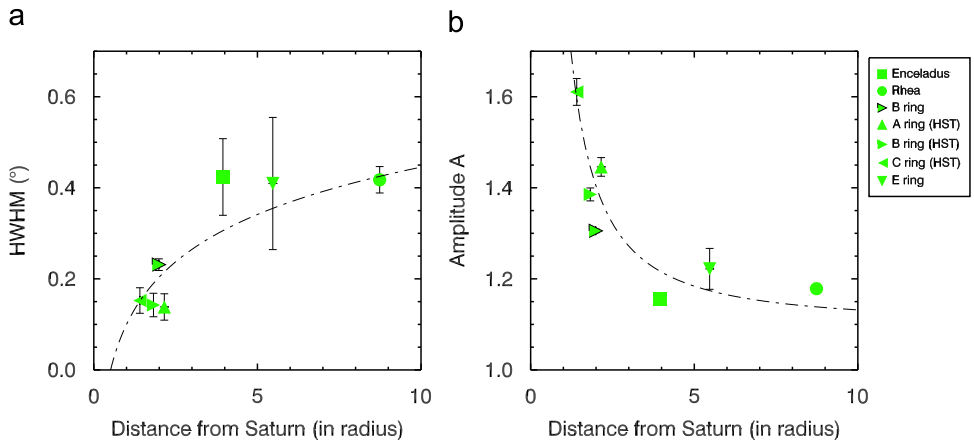

Fig. 9. Variation of the morphological parameters: the amplitude A of the surge (a) and the half-width at half-maximum HWHM (b) derived with the linear-by-parts model with the distance from Saturn. (Distances are taken from Murray and Dermott, 2000.)

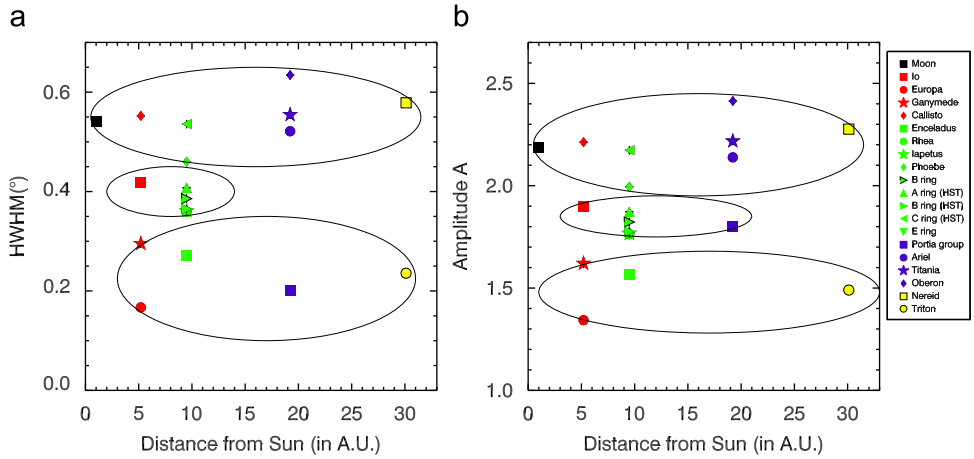

Fig. 10. Variation of the deconvolved morphological parameters: the half-width at half-maximum HWHM (a) and the amplitude A of the surge (b) derived with the logarithmic model fitted by the linear-by-parts model with distance from Saturn. (Distances are taken from Murray and Dermott, 2000.) Solid ellipses in (a) and (b) are arbitrary delimitations of the data points (see text).

In the case of ring particles, the erosion model by ballistic transport of Ip (1983) has been developed and predicted important effects on the radial structure and long-term evolution of the main rings (see also Durisen et al., 1996).

3.4. Study of the deconvolved opposition parameters

With the deconvolved morphological parameters obtained with the method presented in Section 2.3.5, we are now sure that the morphological surge parameters are independent of the distance from the Sun, and thus independent of the "solar size bias". Indeed, in Fig. 10, we represent A and HWHM derived from the linear-by-parts model which fits the logarithmic model as a function of the distance from the Sun and we observe that there is no relation with the heliocentric distance, unlike in Fig. 8 and the results of Bauer et al. (2006). As a consequence, the deconvolution process has successfully removed the solar size bias.

Moreover, we can see that three groups can be distinguished:

(1) A group with the Moon, Callisto, the C ring, Phoebe, the classical Uranian satellites (Ariel, Titania and Oberon) and Nereid. They have large angular widths and amplitudes (HWHM $\gtrsim 0.55^\circ$, Fig. 10a and $A \gtrsim 2.2$, Fig. 10b). We can see that these objects are dark, with low and moderate albedos (Table 5). These satellites are also known to be heavily cratered (Neukum et al., 2001; Zahnle et al., 2003); thus, they do not have intrinsic resurfacing mechanisms. For the case of the resurfacing of Saturn's C ring, it is known that the collisional activity of a ring is controlled by the optical depth τ (Cuzzi and Estrada, 1998). The number of collisions per orbit and per particle is proportional to τ (in the regime of low optical depth, see Wisdom and Tremaine, 1988), and the random velocity in a ring of thickness H is about $H \times \Omega$ (with Ω standing for the local orbital frequency). Since H is a decreasing function of τ, impact velocities are larger in regions of low optical depth. As a result, particles in low optical depth ring regions (such as the C ring) are expected to suffer resurfacing characterized by rare, but somewhat higher-speed, collisions.

(2) A group with Io, Iapetus, Rhea and the bright Saturnian rings characterized by smaller amplitude and angular width: $1.8 \lesssim A \lesssim 1.9$ and HWHM$\sim 0.4^\circ$ (Figs. 10a, b).

(3) A group with Ganymede, Europa, Enceladus and Triton with the smallest amplitude and angular width ($A \lesssim 1.6$, Fig. 10a and HWHM $\lesssim 0.3^\circ$, Fig. 10b). Interestingly for the amplitude, we can see that this group contains some of the brightest surfaces of the satellites of the solar system, with a single-scattering albedo close to $\varpi_0 \sim 0.9$ (however, the Bond albedo of Ganymede is much smaller; see Squyres and Veverka,

1981). These objects are also known to have active resurfacing. Indeed, this was confirmed for Europa, which has a very young surface and perhaps recent geyser-like or volcanic activity (Sullivan et al., 1998; Pappalardo et al., 1998b), and Ganymede, on which the grooved terrains could have formed through tectonism, probably combined with icy volcanism (Pappalardo et al., 1998a; McCord et al., 2001). Present-day resurfacing is also taking place on Enceladus, whose geysers produce the E ring (Porco et al., 2006), and for Triton, which also has geysers (Croft et al., 1995).

This classification seems to suggest that the darkest and oldest surfaces have the largest amplitudes for the surge and that the brightest and youngest surfaces have the smallest amplitudes. However, one might be surprised that the third group does not include Io, which has an intense resurfacing via tidally induced volcanism. Also, the Portia group does not belong to only one group in Fig. 10: it belongs to group 3 for HWHM and to group 2 for the amplitude A. For these two isolated cases, it is possible that the average of photometric phase curves from different satellite regions is responsible for the fact that Io and the Portia group are hard to classify.

4. Discussion

4.1. Implications of the surge parameters of the deconvolved data

By removing the "solar size bias", we can try to physically interpret the amplitude variations versus the single-scattering albedo and link them to the mechanisms proposed to explain the opposition effect. Our study shows a link between the single-scattering albedo and the deconvolved morphological parameters. A linear fit to the deconvolved amplitude is $A = 2.2 - 0.5\varpi_0$ (with a correlation coefficient of -61%) and the linear fit to the deconvolved angular width is $\mathrm{HWHM} = 0.52 - 0.19\varpi_0$ (with a correlation coefficient of -38%). By excluding the Portia group, we find a better correlation coefficient for HWHM: -66%. These correlations are stronger than those previously found with the convolved data. This shows that the "solar size bias" acts to scatter the morphological parameters. As a consequence, the fact that old and dark surfaces with a low resurfacing activity have high deconvolved amplitude whereas the bright and young surfaces with an intense resurfacing activity have low deconvolved amplitude is linked to the single-scattering albedo variations of A. Indeed, the single-scattering albedo is a measure of the brightness of a surface. According to Shkuratov et al. (1999), the amplitude of the coherent-backscattering opposition surge is a decreasing function of increasing regolith grain size. If the morphological amplitude is due to the coherent-backscattering effect (Mishchenko and Dlugach, 1992b; Mishchenko et al., 2006), the dependence of A on ϖ_0 could be understood as a positive correlation between the grain size and the single-scattering albedo. However, in general, the single-scattering albedo would be expected to correlate negatively with grain size (because bigger grains have a longer path length for absorption), so the link between the variation of the morphological amplitude and the grain size is not clear. Moreover, it is possible that the morphological amplitude is not only that of the coherent-backscattering effect but is dominated by both effects: coherent backscatter and shadow hiding, as underlined by Hapke (2002). But it is not possible here to separate the two effects and say which effect is dominant because to definitively separate the coherent-backscatter and shadow-hiding mechanisms, information about the polarization is required (Mishchenko, 1993; Muinonen et al., 2007).

4.2. Implications for the slope of the linear part

The strong correlation of the slope S (in absolute $I/F\,\mathrm{deg}^{-1}$ units) with single-scattering albedo (Fig. 6) implies that the values of the absolute slope S are higher for high-albedo surfaces. A similar trend was previously found for the slope of asteroids (Belskaya and Shevchenko, 2000). It was first interpreted by these authors as a decrease of the absolute slope with albedo, consistent with the analytical model of Helfenstein et al. (1997), which predicted that the amplitude of the shadow hiding must decrease with increasing albedo. However, it must be emphasized that the slope unit in Belskaya and Shevchenko (2000) is the magnitude (note that the scale of the magnitude is not reversed for their graph with the slope—Fig. 4—whereas the other graphs that show the phase curves—Figs. 1 and 2—have a reversed scale for the magnitude, compatible with an I/F scale). So, a decreasing slope in $\mathrm{mag\,deg}^{-1}$ corresponds to an increasing slope in absolute $I/F\,\mathrm{deg}^{-1}$ units. Or, a decreasing slope in $\mathrm{mag\,deg}^{-1}$ corresponds to a decreasing slope in nonabsolute $I/F\,\mathrm{deg}^{-1}$ units. As a consequence, the rings, satellites and asteroids of the solar system have consistent behavior of the absolute slope as a function of the albedo and all lead to the same idea that shadow hiding induces a reinforcement of the absolute values of the slope with increasing albedo. We notice also that a normalized slope (named S' in Section 3.1) gives similar trends with respect to the single-scattering albedo. Then, the slope ($|d(I/F)/d\alpha|$) is still larger for high-albedo objects and increases with increasing albedo, even though the normalized change $|d(I/F)/d\alpha|/(I/F)$. As a result, the positive correlation between the absolute slope and the single-scattering albedo seems to be the strongest trend of the opposition effect in satellites and rings of the solar system and the use of more sophisticated models is needed to understand this trend in terms of filling factor and size distribution.

The results from Fig. 6 are in agreement with the simulations of ray-tracing (Stankevich et al., 1999), which model shadow hiding in a layer of particles. These simulations show that shadow hiding creates a linear part in the phase function from 10° to 40° and that the absolute slope of the linear part becomes steeper when optical depth increases and the filling factor of the layer of particles increases.

How does albedo relate to the optical depth and the filling factor? Previous studies have shown that the albedo and optical depth are highly positively correlated for the rings (see Doyle et al., 1989; Cooke, 1991; Dones et al., 1993). For satellites, optical depth is effectively infinite; since this removes one variable, relating the slope parameter to the nature of the surface is easier for satellites than for rings. Thus we must consider two kinds of objects:

- For rings, where the optical depth is finite, variation of the slope S will be a subtle effect involving both optical depth and filling factor.
- For satellites, which have "solid" surfaces, variations in slope are linked to the filling factor. If the optical depth is invariant for satellites, according to the model of Stankevich et al. (1999), only variations of the filling factor can explain differences of the slope S. However, the notion of filling factor is not well suited for satellites; indeed, a description involving a large-scale roughness, as topography, should be more appropriate.

We noticed that when the optical depth is finite, as for the rings, the effects of slope are stronger with a high albedo than for high-albedo satellites. Consequently the shadow-hiding effect for the ring is more pronounced than for satellites and reflects a

difference between the three-dimensional aspect of a layer of particles in the rings and a planetary regolith.

5. Conclusions

The goal of this paper was to understand the role of the viewing conditions on the morphological parameters of the opposition surge and the role played by the single-scattering albedo on the morphological parameters. We have used three methods to fit the data: first, with a simple morphological model; second, by taking the size of the Sun into account more accurately in the morphological model; and third, by effectively eliminating the size of the Sun in the morphological model.

The results of this study allow us to highlight several facts related to the observations and the mechanisms of the opposition effect in the solar system.

(1) The absolute slope of the linear part (in $I/F\,\mathrm{deg}^{-1}$ absolute units) is an increasing function of single-scattering albedo. Because the slope is negative due to the decrease of the phase function, we can also say that the slope of the linear part of the phase function decreases with increasing single-scattering albedo. Our results are consistent with those of Belskaya and Shevchenko (2000), who find that the phase coefficient β of the phase function of asteroids (in $\mathrm{mag\,deg}^{-1}$ units) decreases when albedo increases. These results confirm the predictions from simulations of shadow-hiding of Stankevich et al. (1999), if we assume that the single-scattering albedo is positively correlated with the optical depth.

(2) We note that the morphological parameters of the surge (A and HWHM) are sensitive to the phase angle coverage, specifically to the smallest phase angles. We have extrapolated observational data points in order to correct the lack of data near the solar angular radius. However, this method needs to be improved, for example by taking the solar angular radius directly into account in the linear-exponential function. We hope that future data at the smallest phase angles will confirm the extrapolated data that we use to perform the "extrapolated linear-exponential" model.

(3) The amplitude and the angular width of the opposition surge are linked to the single-scattering albedo of the surfaces, as already noted in laboratory measurements (Kaasalainen, 2003). Like Belskaya and Shevchenko (2000), we believe that the single-scattering albedo is one of the key physical parameters that constrain the morphological parameters. However, before physically interpreting these results, A and HWHM need to be deconvolved for the "solar size bias" since we have a large dispersion in the relations of $A = f(\varpi_0)$ and $\mathrm{HWHM} = f(\varpi_0)$.

(4) By deconvolving the phase functions for the Sun's angular size effect, we showed that A and HWHM are still correlated with the albedo (with better correlation coefficients). A and HWHM now appear to be independent of the distance from the Sun, unlike their convolved counterparts. Indeed, values of A and HWHM from deconvolved phase functions can be classified into three groups that include a mix of bodies from the inner and the outer solar system. This shows that icy and young surfaces (such as Europa, Io, Enceladus and Triton) have the smallest amplitudes, whereas dark and older surfaces (such as the Moon, Phoebe and the C ring) have the largest amplitudes.

(5) It seems that two effects (the "solar size bias" and the "planetary environmental effect") act together to disperse data taken from different places in the solar system. Moreover, with our technique of deconvolution of phase curves, we see that the "solar size bias" can be removed from A and HWHM, because the deconvolved data have A and HWHM that do not show any trend with distance from the Sun. These arguments strengthen the conclusions that the notion of "ecosystem" for a planetary environment can be the key element determining the opposition effect surge morphology in the solar system.

After our work was complete, we learned of the paper by Schaefer et al. (2009), who quantify the opposition surges of 52 bodies in the outer solar system, primarily by fitting phase curves they measured themselves. Their sample includes bodies orbiting the Sun (dwarf planets, Kuiper belt/scattered disk objects, and centaurs) and 17 satellites. They find that almost all of the bodies have opposition surges dominated by coherent backscattering. They find that "young" surfaces generally have high albedos, gray colors, and shallow surges, while "old" surfaces have low albedos, red colors, and steep surges. They also find that the moons typically have much narrower surges than the bodies orbiting the Sun. Their results appear to be generally compatible with ours.

Our method cannot directly derive the physical properties obtained from the models. First, there is a large set of models, and it seemed more convenient to separate the morphological models from the more physical and sophisticated ones. Second, because the crude spectral resolution of our data set is not appropriate for a majority of physical models which need a fine spectral resolution (for example, in the coherent-backscatter theory, HWHM is linked to the ratio of the wavelength to the free mean path of photons). In addition, coherent backscatter can significantly polarize the observed brightness of a surface, so the polarization phase curves can add crucial and complementary information to that of the unpolarized phase curves. The polarization opposition effect has already been discovered for most of the objects that exhibit a photometric opposition surge (Rosenbush et al., 2002, 2006; Rosenbush and Kiselev, 2005; Belskaya et al., 2008). These discoveries provided almost unequivocal evidence of the interference origin of both opposition phenomena for these objects. More work will need to be done with a large set of satellites of the solar system (see also Mishchenko et al., 2006). Consequently, more investigations need to be provided for this purpose by using color and polarization phase curves.

For future work, which will critically depend on the quality of the observations, first it would be interesting to study the phase functions of the leading and trailing faces of synchronously rotating satellites in order to test the role of the environmental effect more precisely. Indeed, satellites are subject to energy fluxes from electrons, photons and magnetospheric plasma, and ion bombardment, which differ markedly between the leading and trailing sides (Buratti et al., 1988). Consequently, morphological parameters might vary significantly from the leading side to the trailing side for the same satellites. However, the large dispersion in trailing side data (see, for example, Kaasalainen et al., 2001) did not allow us to pursue this comparison. For a future study, we hope to have more accurate data for all of the satellites of the solar system.

Second, to better understand the role of the "planetary environmental effect," a more relevant study would be the comparison of rings with "ringmoons," i.e., small satellites which are in the vicinity of the rings. Several examples of such a ring/ringmoon system are present in the environment of each giant planet:

- for Jupiter: Metis and Adrastea with the main ring (Showalter et al., 1987); Amalthea and Thebe with the Gossamer ring (Burns et al., 1999);

- for Saturn: Pan, Daphnis and Atlas with the outer A ring (Smith et al., 1981; Spitale et al., 2006), Prometheus and Pandora with the F ring (Smith et al., 1981), and Enceladus with the E ring (although Enceladus is the primary source of the E ring, it is not usually called a "ringmoon" Verbiscer et al., 2007);
- for Uranus: Cordelia and Ophelia with the ε ring (French and Nicholson, 1995);
- for Neptune: Galatea with the Adams ring (Porco, 1991).

Unfortunately, opposition phase curves of the small satellites are not generally available because they require multiple observations of faint targets, generally with a high level of background light from the planet and/or rings. However, ringmoons can be observed more easily using groundbased and Earth-orbiting telescopes near the times of ring-plane crossings—e.g. Bosh and Rivkin (1996) and Nicholson et al. (1996) for Saturn and Showalter et al. (2007) and de Pater (2008) for Uranus. In addition, the Cassini extended mission and future missions to the outer solar system may provide phase curves for some of the small satellites. We anticipate that these new data sets and improved photometric models will provide a better understanding of the relation between planetary rings and ring moons in the decades to come.

Acknowledgments

The authors would like to thank S. Kaasalainen, V. Rosenbush and R. French for kindly providing us some of the solar phase curves used here, as well as J. Burns, K. Muinonen, D. Stankevich, and the referees of this paper for useful comments that improved the quality of the paper. This work was supported by the French Centre National de la Recherche Scientifique and the Cassini project.

Appendix A. Refinements to the Sun's angular size effect

To compute the distance from a solar system object to the Sun at any given date, it is not appropriate to use the semi-major axis. We use a series of equations which take into consideration the distance between the Sun and the planet at the approximate date. The heliocentric radius r_p, the distance from the focus of the ellipse (i.e., the Sun) to the planet, is given by

$$r_p = a(1 - e\cos E) \tag{10}$$

where E is the eccentric anomaly, a and e are two of the seven orbital elements which define an ellipse in space: a is the mean distance, or the value of the semi-major axis of the orbit (average Sun to planet distance); e is the eccentricity of the ellipse which describes the orbit (dimensionless); i is the inclination (in degrees), or angle between the plane of the ecliptic (the plane of the Earth's orbit about the Sun) and the plane of the planets orbit; Ω is the longitude of ascending node (in degrees), or the position in the orbit where the elliptical path of the planet passes through the plane of the ecliptic, from below the plane to above the plane; $\tilde{\omega}$ is the longitude of perihelion (in degrees), or the position in the orbit where the planet is closest to the Sun; λ is the mean longitude (in degrees), the position of the planet in the orbit; and M is mean anomaly (in degrees). The mean anomaly gives the planet's angular position for a circular orbit with radius equal to the semi-major axis. It is computed directly from the elements using

$$M = \lambda - \tilde{\omega} \tag{11}$$

Table 6
References for the observational parameters needed to compute the angular size of the Sun $\alpha_\odot$.

Object	Solar angular size $\alpha_\odot$ (°)	Observation time (UT)	References
Moon	0.263	1968 December 24	Whitaker (1969)
Jupiter			
Main ring	0.0506	2000 December 13	Throop et al. (2004)
Io	0.0498	1977 December 15	Lockwood et al. (1980)
Europa	0.0515	1976 **January 1**	Thompson and Lockwood (1992)
Ganymede	0.0499	1971 **May 1**	Blanco and Catalano (1974)
Callisto	0.0515	1976 **January 1**	Thompson and Lockwood (1992)
Saturn			
C ring (HST)	0.0295	2005 January 13	French et al. (2007)
B ring	0.0266	1959 June 26	Franklin and Cook (1965)
B ring (HST)	0.0295	2005 January 13	French et al. (2007)
A ring (HST)	0.0295	2005 January 13	French et al. (2007)
E ring	0.0271	1980 **January 1**	Larson (1984)
Enceladus	0.0287	1997 October 10	Verbiscer et al. (2005)
Rhea	0.0268	1976 January 13	Lockwood et al. (1980)
Iapetus	0.0266	**1972 December**	Franklin and Cook (1974)
Phoebe	0.0295	2005 January 13	Bauer et al. (2006)
Uranus			
Rings	0.0138	1997 July 29	Karkoschka (2001)
Portia *group*	0.0138	1997 July 29	Karkoschka (2001)
Ariel	0.0138	1997 July 29	Karkoschka (2001)
Titania	0.0138	1997 July 29	Karkoschka (2001)
Oberon	0.0138	1997 July 29	Karkoschka (2001)
Neptune			
Fraternité	0.00885	2002 July 27	de Pater et al. (2005)
Egalité	0.00885	2002 July 27	de Pater et al. (2005)
Nereid	0.00889	1998 June 20	Schaefer and Tourtellotte (2001)
Triton	0.00885	**1988 June 20**	Buratti et al. (1991)

Bold text corresponds to observations whose time-of-day was not specified; in these cases we assumed an hourly time of 18:00. In some cases the observations extended over a period of years, so we have chosen one date arbitrarily.

Table 7
Parameters of the limb darkening function of Pierce and Waddell (1961) at similar wavelengths to the observations.

Object	λ_{obs} (nm)	Pierce and Waddell (1961)			
		λ (nm)	a_λ	b_λ	c_λ
Moon	~570	560	0.75079	0.41593	−0.54334
Jupiter					
Main ring	~460	460	0.58274	0.56078	−0.46772
Io	~570	560	0.75079	0.41593	−0.54334
Europa	~500	500	0.68897	0.47873	−0.54651
Ganymede	~600	600	0.78074	0.38427	−0.53777
Callisto	~500	500	0.68897	0.47873	−0.54651
Saturn					
C ring (HST)	672	660	0.83717	0.33283	−0.55400
B ring	~650	640	0.81999	0.34918	−0.55132
B ring (HST)	672	660	0.83717	0.33283	−0.55400
A ring (HST)	672	660	0.83717	0.33283	−0.55400
E ring	~650	640	0.81999	0.34918	−0.55132
Enceladus	439	440	0.49375	0.62584	−0.38974
Rhea	~500	500	0.68897	0.47873	−0.54651
Iapetus	~600	600	0.78074	0.38427	−0.53777
Phoebe	~650	640	0.81999	0.34918	−0.55132
Uranus					
Rings	~500	500	0.68897	0.47873	−0.54651
Portia *group*	~500	500	0.68897	0.47873	−0.54651
Ariel	~600	600	0.78074	0.38427	−0.53777
Titania	~600	600	0.78074	0.38427	−0.53777
Oberon	~600	600	0.78074	0.38427	−0.53777
Neptune					
Fraternité	~500	500	0.68897	0.47873	−0.54651
Egalité	~500	500	0.68897	0.47873	−0.54651
Nereid	~570	560	0.75079	0.41593	−0.54334
Triton	~400	400	0.16732	0.84347	−0.03516

Kepler's second law states that the radius vector of a planet sweeps out equal areas in equal times. The planet must speed up and slow down in its orbit. The true anomaly f gives the planet's actual angular position in its orbit. It is the angle (at the Sun) between perihelion of the orbit and the current location of the planet. To obtain its value, first we compute the eccentric anomaly, E, from M and the eccentricity e by using the "Kepler equation":

$$M = E - e\sin E \tag{12}$$

An expansion to order e^3 of the solution to the "Kepler equation" is

$$E = M + \left(e - \frac{e^3}{8}\right)\sin M + \frac{1}{2}e^2\sin 2M + \frac{3}{8}e^3\sin 3M \tag{13}$$

Now, to find the orbital elements of a planet at a specific date, we use

$$a = a_0 + \dot{a}t \tag{14}$$
$$e = e_0 + \dot{e}t \tag{15}$$
$$i = i_0 + (\dot{a}/3600)t \tag{16}$$
$$\tilde{\omega} = \tilde{\omega}_0 + (\dot{\tilde{\omega}}/3600)t \tag{17}$$
$$\Omega = \Omega_0 + (\dot{\Omega}/3600)t \tag{18}$$
$$\lambda = \lambda_0 + (\dot{\lambda}/3600 + 360N_r)t \tag{19}$$

where t is the observation time (Table 6 in the Appendix) converted into Julian centuries since JD 2451545.0, the quantities with the subscript "0" are the orbital elements at the epoch of J2000 (JD 2451545.0) and the dot quantities are the change per julian century (1 julian century = 31,557,600 s) of the orbital elements (values are taken from Murray and Dermott, 2000). When we have the heliocentric radius at the given observation time, we can compute the solar angular size $\alpha_\odot$ using r_p and $r_\odot$, the radius of the Sun:

$$\alpha_\odot = \arcsin\frac{r_\odot}{r_p} \tag{20}$$

The limb darkening function of Pierce and Waddell (1961) has been used in the past to be convolved with a theoretical opposition effect function (Kawata and Irvine, 1974). Its formula is

$$W(\mu') = a_\lambda + b_\lambda\mu' + c_\lambda\left[1 - \mu'\cdot\log\left(1 + \frac{1}{\mu'}\right)\right] \tag{21}$$

where $\mu' = \cos\theta'$ and θ' varies from 0 to the Sun's angular radius $\alpha_\odot$. a_λ, b_λ and c_λ are coefficients that depend on the wavelength (values are given in Table 7 in the Appendix). We perform a normalized convolution of the limb darkening function to the linear-exponential function $P(\alpha)$ by doing

$$P'(\alpha) = \frac{\int_0^{\alpha_\odot} P(\alpha)\cdot W(\cos\theta')\,d\theta'}{\int_0^{\alpha_\odot} W(\cos\theta')\,d\theta'} \tag{22}$$

References

Bauer, J.M., Grav, T., Buratti, B.J., Hicks, M.D., 2006. The phase curve survey of the irregular Saturnian satellites: a possible method of physical classification. Icarus 184, 181–197.

Belskaya, I.N., Levasseur-Regourd, A.-C., Shkuratov, Y.G., Muinonen, K., 2008. Surface properties of Kuiper belt objects and centaurs from photometry and polarimetry. In: Barucci, M.A., Boehnhardt, H., Cruikshank, D.P., Morbidelli, A. (Eds.), The Solar System Beyond Neptune. University of Arizona Press, Tucson, pp. 115–127.

Belskaya, I.N., Shevchenko, V.G., 2000. Opposition effect of asteroids. Icarus 147, 94–105.

Blanco, C., Catalano, S., 1974. On the photometric variations of the Saturn and Jupiter satellites. Astronomy and Astrophysics 33, 105–111.

Bobrov, M.S., 1970. Physical properties of Saturn's rings. In: Dollfus, A. (Ed.), Surfaces and Interiors of Planets and Satellites. Academic, New York, pp. 376–461.

Bosh, A.S., Rivkin, A.S., 1996. Observations of Saturn's inner satellites during the May 1995 ring-plane crossing. Science 272, 518–521.

Buratti, B.J., 1984. Voyager disk resolved photometry of the Saturnian satellites. Icarus 59, 392–405.

Buratti, B.J., Gibson, J., Mosher, J.A., 1992. CCD photometry of the Uranian satellites. Astronomical Journal 104, 1618–1622.

Buratti, B.J., Lane, A.L., Gibson, J., Burrows, H., Nelson, R.M., Bliss, D., Smythe, W., Garkanian, V., Wallis, B., 1991. Triton's surface properties—a preliminary analysis from ground-based, Voyager photopolarimeter subsystem, and laboratory measurements. Journal of Geophysical Research Supplement 96, 19197–19202.

Buratti, B.J., Nelson, R.M., Lane, A.L., 1988. Surficial textures of the Galilean satellites. Nature 333, 148–151.

Buratti, B.J., Veverka, J., 1985. Photometry of rough planetary surfaces: the role of multiple scattering. Icarus 64, 320–328.

Burns, J.A., Showalter, M.R., Hamilton, D.P., Nicholson, P.D., de Pater, I., Ockert-Bell, M.E., Thomas, P.C., 1999. The formation of Jupiter's faint rings. Science 284, 1146–1150.

Chandrasekhar, S., 1960. Radiative Transfer. Dover, New York.

Colwell, J.E., Esposito, L.W., 1992. Origins of the rings of Uranus and Neptune. I—Statistics of satellite disruptions. Journal of Geophysical Research 97, 10227–10241.

Colwell, J.E., Esposito, L.W., 1993. Origins of the rings of Uranus and Neptune. II—Initial conditions and ring moon populations. Journal of Geophysical Research 98, 7387–7401.

Cooke, M.L., 1991. Saturn's rings: photometric studies of the C ring and radial variation in the Keeler Gap. Unpublished Ph.D. Thesis, Cornell University, Ithaca, NY.

Croft, S.K., Kargel, J.S., Kirk, R.L., Moore, J.M., Schenk, P.M., Strom, R.G., 1995. The geology of Triton. In: Cruikshank, D.P. (Ed.), Neptune and Triton. University of Arizona Press, Tucson, pp. 879–947.

Cuzzi, J.N., Estrada, P.R., 1998. Compositional evolution of Saturn's rings due to meteoroid bombardment. Icarus 132, 1–35.

Déau, E., Charnoz, S., Dones, L., Brahic, A., Porco, C.C., 2009. ISS/Cassini observes the opposition effect in Saturn's rings: I. Morphology of optical phase curves. Icarus submitted in April 2007, under review. Astroph 2009arXiv0902.0289D.

de Pater, I., Gibbard, S.G., Chiang, E., Hammel, H.B., Macintosh, B., Marchis, F., Martin, S.C., Roe, H.G., Showalter, M., 2005. The dynamic Neptunian ring arcs: evidence for a gradual disappearance of Liberté and resonant jump of courage. Icarus 174, 263–272.

de Pater, I., et al., 2008. Progress on analysis of ground-based observations of the ring plane crossings of Uranus. AAS/Division for Planetary Sciences Meeting Abstracts 40, #24.08.
Domingue, D.L., Lockwood, G.W., Thompson, D.T., 1995. Surface textural properties of icy satellites: a comparison between Europa and Rhea. Icarus 115, 228–249.
Domingue, D., Verbiscer, A., 1997. Re-analysis of the solar phase curves of the icy Galilean satellites. Icarus 128, 49–74.
Dones, L., Cuzzi, J.N., Showalter, M.R., 1993. Voyager photometry of Saturn's A ring. Icarus 105, 184–215.
Doyle, L.R., Dones, L., Cuzzi, J.N., 1989. Radiative transfer modeling of Saturn's outer B ring. Icarus 80, 104–135.
Durisen, R.H., Bode, P.W., Dyck, S.G., Cuzzi, J.N., Dull, J.D., White, J.C., 1996. Ballistic transport in planetary ring systems due to particle erosion mechanisms. Icarus 124, 220–236.
Esposito, L.W., Lumme, K., Benton, W.D., Martin, L.J., Ferguson, H.M., Thompson, D.T., Jones, S.E., 1979. International planetary patrol observations of Saturn's rings. II—Four color phase curves and their analysis. Astronomical Journal 84, 1408–1415.
Ferrari, C., Brahic, A., 1994. Azimuthal brightness asymmetries in planetary rings. 1: Neptune's arcs and narrow rings. Icarus 111, 193–210.
Franklin, F.A., Cook, F.A., 1965. Optical properties of Saturn's rings. II. Two-color phase curves of the 2 bright rings. Astronomical Journal 70, 704–720.
Franklin, F.A., Cook, A.F., 1974. Photometry of Saturn's satellites—the opposition effect of Iapetus at maximum light and the variability of Titan. Icarus 23, 355–362.
French, R.G., Nicholson, P.D., 1995. Edge waves and librations in the Uranus epsilon ring. Bulletin of the American Astronomical Society 27, 857.
French, R.G., Verbiscer, A., Salo, H., McGhee, C., Dones, L., 2007. Saturn's rings at true opposition. Publications of the Astronomical Society of the Pacific 119, 623–642.
Hapke, B., 1984. Bidirectional reflectance spectroscopy. III—Correction for macroscopic roughness. Icarus 59, 41–59.
Hapke, B., 1986. Bidirectional reflectance spectroscopy. IV—The extinction coefficient and the opposition effect. Icarus 67, 264–280.
Hapke, B., 2002. Bidirectional reflectance spectroscopy V—the coherent backscatter opposition effect and anisotropic scattering. Icarus 157, 523–534.
Hapke, B., Dimucci, D., Nelson, R., Smythe, W., 1996. The nature of the opposition effect in frost, vegetation and soils. In: Lunar and Planetary Institute Conference Abstracts. Lunar and Planetary Institute Technical Report, vol. 27, p. 491.
Harris, A.W., Young, J.W., Bowell, E., Martin, L.J., Millis, R.L., Poutanen, M., Scaltriti, F., Zappala, V., Schober, H.J., Debehogne, H., Zeigler, K.W., 1989a. Photoelectric observations of asteroids 3, 24, 60, 261, and 863. Icarus 77, 171–186.
Harris, A.W., Young, J.W., Contreiras, L., Dockweiler, T., Belkora, L., Salo, H., Harris, W.D., Bowell, E., Poutanen, M., Binzel, R.P., Tholen, D.J., Wang, S., 1989b. Phase relations of high albedo asteroids—the unusual opposition brightening of 44 Nysa and 64 Angelina. Icarus 81, 365–374.
Helfenstein, P., Veverka, J., Hillier, J., 1997. The lunar opposition effect: a test of alternative models. Icarus 128, 2–14.
Ip, W.-H., 1983. Collisional interactions of ring particles—the ballistic transport process. Icarus 54, 253–262.
Irvine, W.M., 1966. The shadowing effect in diffuse reflection. Journal of Geophysical Research 71, 2931–2937.
Kaasalainen, S., 2003. Laboratory photometry of planetary regolith analogs. I. Effects of grain and packing properties on opposition effect. Astronomy and Astrophysics 409, 765–769.
Kaasalainen, S., Muinonen, K., Piironen, J., 2001. Comparative study on opposition effect of icy solar system objects. Journal of Quantitative Spectroscopy and Radiative Transfer 70, 529–543.
Karkoschka, E., 2001. Comprehensive photometry of the rings and 16 satellites of Uranus with the Hubble Space Telescope. Icarus 151, 51–68.
Kawata, Y., Irvine, W.M., 1974. Models of Saturn's rings which satisfy the optical observations. In: Woszczyk, A., Iwaniszewska, C. (Eds.), Exploration of the Planetary System. IAU Symposium 65, pp. 441–464.
Kulyk, I., 2008. Saturnian icy satellites: disk-integrated observations of the brightness opposition surge at low phase angles. Planetary and Space Science 56, 386–397.
Larson, S., 1984. Summary of optical ground-based E ring observations at the University of Arizona. In: Greenberg, R., Brahic, A. (Eds.), IAU Colloquium 75: Planetary Rings, pp. 111–114.
Lee, P., Helfenstein, P., Veverka, J., McCarthy, D., 1992. Anomalous-scattering region on Triton. Icarus 99, 82–97.
Lissauer, J.J., Squyres, S.W., Hartmann, W.K., 1988. Bombardment history of the Saturn system. Journal of Geophysical Research 93, 13776–13804.
Lockwood, G.W., Thompson, D.T., Lumme, K., 1980. A possible detection of solar variability from photometry of Io, Europa, Callisto, and Rhea, 1976–1979. Astronomical Journal 85, 961–968.
Lumme, K., Irvine, W.M., 1976. Photometry of Saturn's rings. Astronomical Journal 81, 865–893.
Lumme, K., Peltoniemi, J., Irvine, W.M., 1990. Some photometric techniques for atmosphereless solar system bodies. Advances in Space Research 10, 187–193.
McCord, T.B., Hansen, G.B., Hibbitts, C.A., 2001. Hydrated salt minerals on Ganymede's surface: evidence of an ocean below. Science 292, 1523–1525.
McEwen, A.S., Soderblom, L.A., Johnson, T.V., Matson, D.L., 1988. The global distribution, abundance, and stability of SO_2 on Io. Icarus 75, 450–478.
Millis, R.L., Thompson, D.T., 1975. UBV photometry of the Galilean satellites. Icarus 26, 408–419.
Mishchenko, M.I., 1992. The angular width of the coherent back-scatter opposition effect—an application to icy outer planet satellites. Astrophysics and Space Science 194, 327–333.
Mishchenko, M.I., 1993. On the nature of the polarization opposition effect exhibited by Saturn's rings. Astrophysical Journal 411, 351–361.
Mishchenko, M.I., Dlugach, Z.M., 1992a. Can weak localization of photons explain the opposition effect of Saturn's rings? Monthly Notices of the Royal Astronomical Society 254, 15P–18P.
Mishchenko, M.I., Dlugach, Z.M., 1992b. The amplitude of the opposition effect due to weak localization of photons in discrete disordered media. Astrophysics and Space Science 189, 151–154.
Mishchenko, M.I., Rosenbush, V.K., Kiselev, N.N., 2006. Weak localization of electromagnetic waves and opposition phenomena exhibited by high-albedo atmosphereless solar system objects. Applied Optics 45, 4459–4463.
Morrison, D., Morrison, N.D., Lazarewicz, A.R., 1974. Four-color photometry of the Galilean satellites. Icarus 23, 399–416.
Muinonen, K., Zubko, E., Tyynelä, J., Shkuratov, Y.G., Videen, G., 2007. Light scattering by Gaussian random particles with discrete-dipole approximation. Journal of Quantitative Spectroscopy and Radiative Transfer 106, 360–377.
Müller, G., 1885. Resultate aus Helligkeitsmessungen des Planeten Saturn. Astronomische Nachrichten 110, 225–232.
Murray, C.D., Dermott, S.F., 2000. Solar System Dynamics. Cambridge University Press, UK ISBN 0521575974.
Nelson, R.M., Hapke, B.W., Smythe, W.D., Spilker, L.J., 2000. The opposition effect in simulated planetary regoliths. Reflectance and circular polarization ratio change at small phase angle. Icarus 147, 545–558.
Neukum, G., Ivanov, B.A., Hartmann, W.K., 2001. Cratering records in the inner solar system in relation to the lunar reference system. Space Science Reviews 96, 55–86.
Nicholson, P.D., Showalter, M.R., Dones, L., French, R.G., Larson, S.M., Lissauer, J.J., McGhee, C.A., Sicardy, B., Seitzer, P., Danielson, G.E., 1996. Observations of Saturn's ring-plane crossing in August and November. Science 272, 509–516.
Pang, K.D., Voge, C.C., Rhoads, J.W., Ajello, J.M., 1983. Saturn's E-ring and satellite Enceladus. In: Lunar and Planetary Institute Conference Abstracts. Lunar and Planetary Institute Technical Report, vol. 14, pp. 592–593.
Pappalardo, R.T., Head, J.W., Collins, G.C., Kirk, R.L., Neukum, G., Oberst, J., Giese, B., Greeley, R., Chapman, C.R., Helfenstein, P., Moore, J.M., McEwen, A., Tufts, B.R., Senske, D.A., Breneman, H.H., Klaasen, K., 1998a. Grooved terrain on Ganymede: first results from Galileo high-resolution imaging. Icarus 135, 276–302.
Pappalardo, R.T., Head, J.W., Greeley, R., Sullivan, R.J., Pilcher, C., Schubert, G., Moore, W.B., Carr, M.H., Moore, J.M., Belton, M.J.S., Goldsby, D.L., 1998b. Geological evidence for solid-state convection in Europa's ice shell. Nature 391, 365–368.
Pierce, A.K., Waddell, J.H., 1961. Analysis of limb darkening observations. Memoirs of the Royal Astronomical Society 63, 89–112.
Porco, C.C., 1991. An explanation for Neptune's ring arcs. Science 253, 995–1001.
Porco, C.C., Helfenstein, P., Thomas, P.C., Ingersoll, A.P., Wisdom, J., West, R., Neukum, G., Denk, T., Wagner, R., Roatsch, T., Kieffer, S., Turtle, E., McEwen, A., Johnson, T.V., Rathbun, J., Veverka, J., Wilson, D., Perry, J., Spitale, J., Brahic, A., Burns, J.A., DelGenio, A.D., Dones, L., Murray, C.D., Squyres, S., 2006. Cassini observes the active south pole of Enceladus. Science 311, 1393–1401.
Poulet, F., Cuzzi, J.N., French, R.G., Dones, L., 2002. A study of Saturn's ring phase curves from HST observations. Icarus 158, 224–248.
Psarev, V., Ovcharenko, A., Shkuratov, Y., Belskaya, I., Videen, G., 2007. Photometry of particulate surfaces at extremely small phase angles. Journal of Quantitative Spectroscopy and Radiative Transfer 106, 455–463.
Rosenbush, V.K., Kiselev, N.N., 2005. Polarization opposition effect for the Galilean satellites of Jupiter. Icarus 179, 490–496.
Rosenbush, V., Kiselev, N., Avramchuk, V., Mishchenko, M., 2002. Photometric and polarimetric opposition phenomena exhibited by solar system bodies. In: Videen, G., Kocifaj, M. (Eds.), Optics of Cosmic Dust. Kluwer, Dordrecht, Netherlands, pp. 191–224.
Rosenbush, V., Kiselev, N., Avramchuk, V., 2006. Similarity and diversity in photometric and polarimetric opposition effects of small solar system bodies. Journal of Quantitative Spectroscopy and Radiative Transfer 100, 325–339.
Rougier, G., 1933. Photometrie photoelectrique globale de la lune. Annales de l'Observatoire de Strasbourg 2, 203–339.
Schaefer, B.E., Tourtellotte, S.W., 2001. Photometric light curve for Nereid in 1998: a prominent opposition surge. Icarus 151, 112–117.
Schaefer, B.E., Rabinowitz, D.L., Tourtellotte, S.W., 2009. The diverse solar phase curves of distant icy bodies II. The cause of the opposition surges and their correlations. Astronomical Journal 137, 129–144.
Seeliger, H., 1884. Zur Photometrie des Saturnringes. Astronomische Nachrichten 109, 305–314.
Shkuratov, I.G., 1991. The effect of the finiteness of the angular dimensions of a light source on the magnitude of the opposition effect of the luminosity of atmosphereless bodies. Astronomicheskii Vestnik 25, 71–75.
Shkuratov, Y.G., Kreslavsky, M.A., Ovcharenko, A.A., Stankevich, D.G., Zubko, E.S., Pieters, C., Arnold, G., 1999. Opposition effect from clementine data and mechanisms of backscatter. Icarus 141, 132–155.
Showalter, M.R., Burns, J.A., Cuzzi, J.N., Pollack, J.B., 1987. Jupiter's ring system—new results on structure and particle properties. Icarus 69, 458–498.

Showalter, M.R., Cuzzi, J.N., Larson, S.M., 1991. Structure and particle properties of Saturn's E ring. Icarus 94, 451–473.
Showalter, M.R., Lissauer, J.J., French, R.G., Hamilton, D.P., Nicholson, P.D., de Pater, I., 2007. HST observations of the Uranian ring plane crossing: early results. Bulletin of the American Astronomical Society 38, 427.
Simonelli, D.P., Kay, J., Adinolfi, D., Veverka, J., Thomas, P.C., Helfenstein, P., 1999. Phoebe: albedo map and photometric properties. Icarus 138, 249–258.
Smith, B.A., Soderblom, L., Beebe, R.F., Boyce, J.M., Briggs, G., Bunker, A., Collins, S.A., Hansen, C., Johnson, T.V., Mitchell, J.L., Terrile, R.J., Carr, M.H., Cook, A.F., Cuzzi, J.N., Pollack, J.B., Danielson, G.E., Ingersoll, A.P., Davies, M.E., Hunt, G.E., Masursky, H., Shoemaker, E.M., Morrison, D., Owen, T., Sagan, C., Veverka, J., Strom, R., Suomi, V.E., 1981. Encounter with Saturn–Voyager 1 imaging science results. Science 212, 163–191.
Spitale, J.N., Jacobson, R.A., Porco, C.C., Owen Jr., W.M., 2006. The orbits of Saturn's small satellites derived from combined historic and Cassini imaging observations. Astronomical Journal 132, 692–710.
Squyres, S.W., Veverka, J., 1981. Voyager photometry of surface features on Ganymede and Callisto. Icarus 46, 137–155.
Stankevich, D.G., Shkuratov, Y.G., Muinonen, K., 1999. Shadow hiding effect in inhomogeneous layered particulate media. Journal of Quantitative Spectroscopy and Radiative Transfer 63, 445–448.
Sullivan, R., Greeley, R., Homan, K., Klemaszewski, J., Belton, M.J.S., Carr, M.H., Chapman, C.R., Tufts, R., Head, J.W., Pappalardo, R., Moore, J., Thomas, P., 1998. Episodic plate separation and fracture infill on the surface of Europa. Nature 391, 371–373.
Thomas, P., Veverka, J., Helfenstein, P., 1991. Voyager observations of Nereid. Journal of Geophysical Research 96, 19253–19259.
Thompson, D.T., Lockwood, G.W., 1992. Photoelectric photometry of Europa and Callisto 1976–1991. Journal of Geophysical Research 97, 14761–14772.
Throop, H.B., Porco, C.C., West, R.A., Burns, J.A., Showalter, M.R., Nicholson, P.D., 2004. The jovian rings: new results derived from Cassini, Galileo, Voyager, and Earth-based observations. Icarus 172, 59–77.
Verbiscer, A.J., French, R.G., McGhee, C.A., 2005. The opposition surge of Enceladus: HST observations 338–1022 nm. Icarus 173, 66–83.
Verbiscer, A., French, R., Showalter, M., Helfenstein, P., 2007. Enceladus: cosmic graffiti artist caught in the act. Science 315, 815.
Verbiscer, A.J., Veverka, J., 1989. Albedo dichotomy of Rhea-Hapke analysis of Voyager photometry. Icarus 82, 336–353.
Verbiscer, A.J., Veverka, J., 1990. Scattering properties of natural snow and frost—comparison with icy satellite photometry. Icarus 88, 418–428.
Verbiscer, A., Veverka, J., 1991. Detection of albedo markings on Enceladus. Bulletin of the American Astronomical Society 23, 1168.
Veverka, J., Thomas, P., Helfenstein, P., Brown, R.H., Johnson, T.V., 1987. Satellites of Uranus-disk-integrated photometry from Voyager imaging observations. Journal of Geophysical Research 92, 14895–14904.
Whitaker, E.A., 1969. An investigation of the Lunar Heiligenschein. NASA Special Publication 201, 38–39.
Wisdom, J., Tremaine, S., 1988. Local simulations of planetary rings. Astronomical Journal 95, 925–940.
Zahnle, K., Schenk, P., Levison, H., Dones, L., 2003. Cratering rates in the outer solar system. Icarus 163, 263–289.